


High-harmonic generation in graphene under the application of a DC electric current: From perturbative to nonperturbative regime

Minoru Kanega^{✉*} and Masahiro Sato[†]

Department of Physics, Chiba University, Chiba 263-8522, Japan

 (Received 5 March 2024; revised 2 June 2024; accepted 17 June 2024; published 12 July 2024)

We theoretically investigate high-harmonic generation (HHG) in honeycomb-lattice graphene models when subjected to a DC electric field. By integrating the quantum master equation with the Boltzmann equation, we develop a numerical method to compute laser-driven dynamics in many-electron lattice systems under DC electric current. The method enables us to treat both the weak-laser (perturbative) and intense-laser (nonperturbative) regimes in a unified way, accounting for the experimentally inevitable dissipation effects. From it, we obtain the HHG spectra and analyze their dependence on laser frequency, laser intensity, laser-field direction, and DC current strength. We show that the dynamical and static symmetries are partially broken by a DC current or staggered potential term, and such symmetry breakings drastically change the shape of the HHG spectra, especially in terms of the presence or absence of $(2n + 1)$ th-, $2n$ th-, or $3n$ th-order harmonics ($n \in \mathbb{Z}$). The laser intensity, frequency, and polarization are also shown to affect the shape of the HHG spectra. Our findings indicate that HHG spectra in conducting electron systems can be quantitatively or qualitatively controlled by tuning various external parameters, and DC electric current is used as such an efficient parameter.

DOI: [10.1103/PhysRevB.110.035303](https://doi.org/10.1103/PhysRevB.110.035303)

I. INTRODUCTION

In the past few decades, nonlinear optical responses in solid-state electronic systems have seen remarkable growth thanks to the development of laser techniques. Various laser-driven nonequilibrium phenomena have been explored including high-harmonic generation (HHG) [1–5], photorectification effects [6–13], Floquet engineering [14–20], and others. Among them, HHG is a simple phenomenon in which a system subjected to intense light of frequency Ω emits light with different frequencies $n\Omega$, as shown in Fig. 1(a). It is relatively easily detectable in experiments compared to other nonlinear optical effects. Though the HHG research had focused on atomic gas systems in the 1990s [21–26], its targets have been expanded to solid-state systems since the 2010s, such as semiconductors [27–36], superconductors [37], semimetals [38–41], strongly correlated electrons [42–45], magnetic insulators [46–51], etc.

It is well known that even-order harmonics of $n = 2, 4, 6, \dots$ are all generally suppressed in solid-state electronic systems with spatial inversion symmetry [52]. This fact leads to an intriguing question: How can one observe/control these suppressed responses? HHG also provides a means to extract light of particular beneficial frequencies. Therefore, addressing the above question becomes vital from both scientific and application perspectives. One viable strategy is to use inversion-asymmetric systems, like p - n junctions [53], perovskite ferroelectrics [54], and Weyl semimetals [55–58]. The inversion asymmetry in these systems generates even-order

harmonics in general, and this research direction has long been thriving. For instance, p - n junctions show potential for solar energy conversion through the $n = 0$ light-induced electric potential [53]. Similarly, the nonlinear optical responses in Weyl semimetals are subjects of intensive study [55–58].

On the other hand, even for inversion-symmetric materials, some extrinsic means can be employed to break the inversion symmetry. Applying a DC current is an effective way to achieve the breakdown. Building on this idea, current-induced second-harmonic generation has been investigated theoretically [59–63] and reported experimentally in materials like Si [64], GaAs [65], graphene [66,67], superconducting NbN [68], and others.

It is noteworthy that both DC current and laser light push the system out of equilibrium. Namely, the application of DC current generally increases complexity in laser-driven systems, making computational predictions daunting. Consequently, so far, only second-harmonic generation spectra have been computed within perturbative ways in most of the previous works for systems under the application of both laser and DC current [59–63]. However, the perturbation theories generally become less feasible when laser intensity grows. Therefore, for HHG in DC-current-driven systems, it is significant to develop a theoretical method that analyzes both perturbative (weak laser) and nonperturbative (strong laser) ranges.

In this paper, motivated by the above backgrounds, we theoretically investigate HHG in honeycomb-lattice graphene models when subjected to a DC electric field. Combining the quantum master equation [48,49,69–72] with the Boltzmann equation [73], we develop numerical methods to quantitatively compute the laser-driven time evolution of observables in many-electron lattice systems under DC electric current,

*Contact author: m.kanega.phys@chiba-u.ac.jp

†Contact author: sato.phys@chiba-u.ac.jp

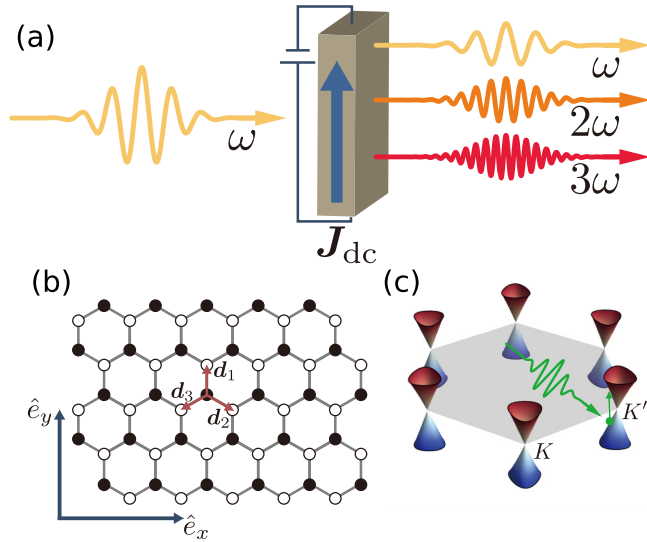


FIG. 1. (a) Schematic diagram of high-harmonic generation in solids under the application of a DC current. (b) Top view of the two-dimensional honeycomb lattice of graphene, whose unit cell includes A- and B-sublattice sites (black and white circles). x and y axes are defined, respectively, by the unit vectors \hat{e}_x and \hat{e}_y . Vectors \mathbf{d}_1 , \mathbf{d}_2 , and \mathbf{d}_3 connect a site on A sublattice and one of the three nearest-neighbor sites. (c) A typical electronic band structure of graphene in the wave-vector space. Blue and red Dirac cones represent, respectively, the valence and conduction bands, and they are located at $\mathbf{K} = \frac{2\pi}{3\sqrt{3}a}(1, \sqrt{3})$ and $\mathbf{K}' = \frac{2\pi}{3\sqrt{3}a}(-1, \sqrt{3})$ points.

and we demonstrate the HHG spectra and their dependence on laser frequency, laser intensity, and DC current strength while accounting for the experimentally inevitable dissipation effects. Our findings indicate that the HHG spectra undergo significant modifications due to dynamical symmetry breaking induced by the applied DC current. Additionally, we observe that nonperturbative effects become pronounced when the laser is strong, leading to a marked alteration in the laser frequency dependence of the HHG spectra.

The remaining part of the paper is organized as follows. In Sec. II, we introduce the formalism of the combination with the master equation and the Boltzmann equation, which describes the time evolution of laser and DC-current induced nonequilibrium states in many-electron systems. We comment on some advantages of the master equation in Sec. III F. The main numerical results based on the master equation are in Sec. III. Section III A reveals that the HHG spectrum is modulated by a DC current, leading to even-order harmonic responses. The section also delves into the DC current dependence of the HHG spectra. In Sec. III B, we explore the influence of laser frequency on the HHG spectra, emphasizing the pronounced differences between the perturbative and nonperturbative regimes. Furthermore, we underscore the significant role of intraband dynamics in the nonperturbative regime. Section III C examines the relationship between laser intensity and the HHG spectra, showing that the crossover between the perturbative and nonperturbative regimes occurs depending on the chemical potential. Section III D discusses the characteristics of the HHG spectrum in the presence of a staggered potential (i.e., the effects of a finite band gap).

When the system is subjected to an intense laser, the interplay between inter- and intraband dynamics in different polarization directions results in intricate shifts in the HHG spectra. Section III E outlines the variations in the HHG spectra under extremely high laser intensities. Finally, in Sec. IV, we summarize our results and make concluding remarks. We discuss some theoretical details associated with dynamical symmetry and the master equation in the Appendixes.

II. MODEL AND METHOD

A. Model and observable

We focus on a model of single-layered graphene [74,75] with A and B sublattices [black and white circles in Fig. 1(b)]. The tight-binding Hamiltonian is given by

$$\begin{aligned} \hat{H}_0 = & -t_0 \sum_{\mathbf{r}} \sum_{j=1,2,3} (\hat{b}_{\mathbf{r}+\mathbf{d}_j}^\dagger \hat{a}_{\mathbf{r}} + \hat{a}_{\mathbf{r}}^\dagger \hat{b}_{\mathbf{r}+\mathbf{d}_j}) \\ & + \Delta \sum_{\mathbf{r}} (\hat{a}_{\mathbf{r}}^\dagger \hat{a}_{\mathbf{r}} - \hat{b}_{\mathbf{r}+\mathbf{d}_1}^\dagger \hat{b}_{\mathbf{r}+\mathbf{d}_1}), \end{aligned} \quad (1)$$

where \mathbf{d}_j , the position vectors pointing to the three nearest-neighbor sites from each A site of the hexagonal plaquette, are given by

$$\begin{aligned} \mathbf{d}_1 &= a(0, 1), \\ \mathbf{d}_2 &= a\left(\cos\left(\frac{\pi}{6}\right), -\sin\left(\frac{\pi}{6}\right)\right), \\ \mathbf{d}_3 &= a\left(-\cos\left(\frac{\pi}{6}\right), -\sin\left(\frac{\pi}{6}\right)\right), \end{aligned} \quad (2)$$

with a being a lattice constant. The vector \mathbf{r} represents each position of sublattice A. The fermionic operator $\hat{a}_{\mathbf{r}}$ ($\hat{a}_{\mathbf{r}}^\dagger$) annihilates (creates) an electron at position \mathbf{r} for the sublattice A. The fermionic one $\hat{b}_{\mathbf{r}}$ ($\hat{b}_{\mathbf{r}}^\dagger$) is defined similarly for the sublattice B. They satisfy the anticommutation relations $\{\hat{a}_{\mathbf{r}}, \hat{a}_{\mathbf{r}'}\} = \{\hat{b}_{\mathbf{r}}, \hat{b}_{\mathbf{r}'}\} = \{\hat{a}_{\mathbf{r}}, \hat{b}_{\mathbf{r}'}\} = \{\hat{a}_{\mathbf{r}}, \hat{b}_{\mathbf{r}}^\dagger\} = 0$ and $\{\hat{a}_{\mathbf{r}}, \hat{a}_{\mathbf{r}}^\dagger\} = \{\hat{b}_{\mathbf{r}}, \hat{b}_{\mathbf{r}}^\dagger\} = \delta_{\mathbf{r},\mathbf{r}'}$. The first term in \hat{H}_0 describes the nearest-neighbor electron hopping between two sublattices A and B with transfer integral t_0 , and the second term represents an on-site staggered potential with a band-gap energy Δ . For graphene, transfer integral t_0 is estimated as $t_0 = 2.7$ eV [74,76] and Δ is usually negligible.

By the Fourier transformation, $\hat{a}_{\mathbf{r}} = \frac{1}{\sqrt{N}} \sum_{\mathbf{k}} \tilde{a}_{\mathbf{k}} e^{-i\mathbf{k}\cdot\mathbf{r}}$, $\hat{b}_{\mathbf{r}} = \frac{1}{\sqrt{N}} \sum_{\mathbf{k}} \tilde{b}_{\mathbf{k}} e^{-i\mathbf{k}\cdot\mathbf{r}}$, where N is the total number of unit cells, the Hamiltonian \hat{H}_0 is expressed in the following bilinear form: $\hat{H}_0 = \sum_{\mathbf{k}} \mathbf{C}_k^\dagger \hat{M}(\mathbf{k}) \mathbf{C}_k$, where $\mathbf{C}_k = (\tilde{a}_{\mathbf{k}} \ \tilde{b}_{\mathbf{k}})^\top$ and $\hat{M}(\mathbf{k}) = h_k^x \sigma_x + h_k^y \sigma_y + h_k^z \sigma_z$ with $(h_k^x, h_k^y, h_k^z) = (-t_0 \sum_{j=1}^3 \cos(\mathbf{k} \cdot \mathbf{d}_j), t_0 \sum_{j=1}^3 \sin(\mathbf{k} \cdot \mathbf{d}_j), \Delta)$ and $\sigma_{x,y,z}$ being Pauli matrices. Through unitary transformation $(\xi_{\mathbf{k}} \ \zeta_{\mathbf{k}}) = U_{\mathbf{k}}^\dagger \mathbf{C}_k$ with new fermion operators $\xi_{\mathbf{k}}$ and $\zeta_{\mathbf{k}}$, the Hamiltonian is diagonalized as $\hat{H}_0 = \sum_{\mathbf{k}} \varepsilon(\mathbf{k}) (\xi_{\mathbf{k}}^\dagger \xi_{\mathbf{k}} - \zeta_{\mathbf{k}}^\dagger \zeta_{\mathbf{k}})$, with the energy dispersion $\varepsilon(\mathbf{k}) = \sqrt{(h_k^x)^2 + (h_k^y)^2 + (h_k^z)^2}$. This dispersion has the Dirac cones at the $\mathbf{K} = \frac{2\pi}{3\sqrt{3}a}(1, \sqrt{3})$ and $\mathbf{K}' = \frac{2\pi}{3\sqrt{3}a}(-1, \sqrt{3})$ points when $\Delta = 0$ as shown in Fig. 1(c). We note that around the \mathbf{K} (\mathbf{K}') point, the energy dispersion is approximated to $E_{\mathbf{K}(\mathbf{K}')+\mathbf{k}} \approx \pm \hbar v_F |\mathbf{k}|$ with the Fermi velocity

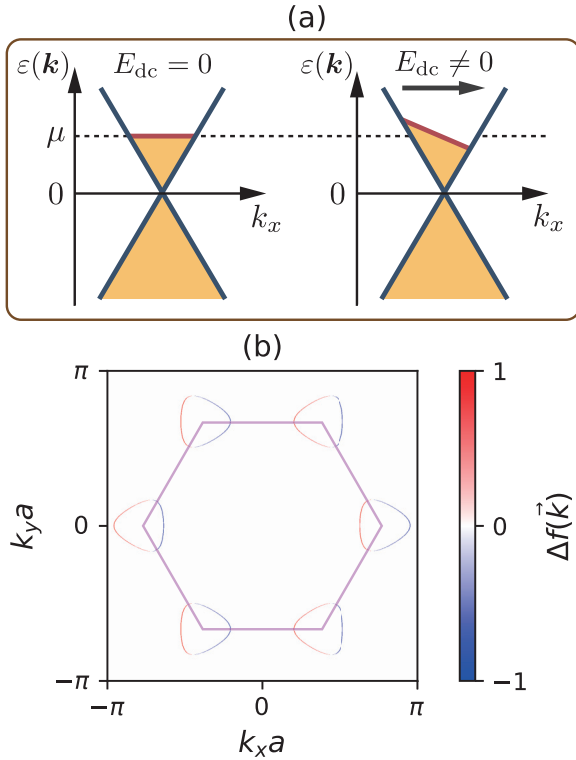


FIG. 2. (a) k -space schematic image of DC-current-induced steady state and equilibrium state near a Dirac point on $k_y = 0$ in the case of zero temperature, $\mu > 0$ and $\Delta = 0$. DC electric field E_{dc} is parallel to the x axis. Yellow region means that electrons are occupied. (b) The difference $\Delta f(\mathbf{k}) = f_{ss}(\mathbf{k}) - f_0(\mathbf{k})$ in the momentum space at zero temperature. Parameters are set to $\mu/t_0 = 0.7$, $\delta_{dc}a = 0.01$, and $\Delta = 0$.

$v_F = \sqrt{3}at_0/(2\hbar)$ and Dirac's constant \hbar . We set $\hbar = 1$ throughout the paper.

The operators $\{\xi_k\}$ and $\{\zeta_k\}$, respectively, correspond to fermionic annihilation operators on the conduction and valence bands. When a chemical potential $\mu = 0$ [see the left panel of Fig. 2(a)], the ground state is given by $|\text{gs}\rangle = \otimes_k |g_k\rangle$, where $|g_k\rangle = \zeta_k^\dagger |0_k\rangle = (-v_k \tilde{a}_k^\dagger + u_k \tilde{b}_k^\dagger) |0_k\rangle$, with $(u_k, v_k) = (\sqrt{[1 + \hbar_k^z/\varepsilon(\mathbf{k})]}/2, \Delta_k \sqrt{[1 - \hbar_k^z/\varepsilon(\mathbf{k})]}/2/|\Delta_k|}$, $\Delta_k = \hbar_k^x - i\hbar_k^y$, and $|0_k\rangle$ is the Fock vacuum for electrons (ζ_k, ξ_k). The one-electron state occupying the conduction band at wave vector \mathbf{k} is given by $|e_k\rangle = \xi_k^\dagger |0_k\rangle = (u_k \tilde{a}_k^\dagger + v_k^* \tilde{b}_k^\dagger) |0_k\rangle$. As one will see later, we use $\{|e_k\rangle, |g_k\rangle\}$ as the basis of time evolution. In the present work, as we will explain in more detail in Sec. II B, we focus on the optical response in a low- or intermediate-energy regime with $0.2 \lesssim \mu/t_0 \lesssim 1.0$, in which ‘‘Dirac’’ electrons around \mathbf{K} and \mathbf{K}' are mainly photoexcited.

We adopt the Peierls-phase formalism to consider the laser-driven dynamics. The time-dependent Hamiltonian with light-matter coupling is given by

$$\begin{aligned} \hat{H}(t) = & - \sum_{r,j} (t_{r,r+d_j}(t) \hat{b}_{r+d_j}^\dagger \hat{a}_r + t_{r+d_j,r}(t) \hat{a}_r^\dagger \hat{b}_{r+d_j}) \\ & + \Delta \sum_r (\hat{a}_r^\dagger \hat{a}_r - \hat{b}_{r+d_1}^\dagger \hat{b}_{r+d_1}), \end{aligned} \quad (3)$$

where $t_{r,r+d_j}(t)$ is the hopping amplitude with Peierls substitution

$$t_{r,r+d_j}(t) = t_0 \exp\left(-ie \int_r^{r+d_j} \mathbf{A}(t) \cdot d\mathbf{r}\right). \quad (4)$$

Here, e is the elementary charge, $\mathbf{A}(t)$ is a vector potential, and the AC electric field of laser $\mathbf{E}(t)$ in the Coulomb gauge is related to $\mathbf{A}(t)$ via the relation $\mathbf{E}(t) = -\frac{\partial \mathbf{A}(t)}{\partial t}$. The Fourier-space representation of the Hamiltonian $\hat{H}(t)$ is given by $\hat{H}(t) = \sum_{\mathbf{k}} \hat{H}_{\mathbf{k}}(t) = \sum_{\mathbf{k}} \mathbf{C}_{\mathbf{k}}^\dagger \mathbf{M}[\mathbf{k} + e\mathbf{A}(t)] \mathbf{C}_{\mathbf{k}}$. We note that, though under the irradiation of a laser, the Hamiltonian $\hat{H}(t)$ is still \mathbf{k} -diagonal like \hat{H}_0 . This is because we now simply apply a spatially uniform laser to the graphene model. Therefore, as we will discuss in Sec. II C, we can independently compute the time evolution of the density matrix at each \mathbf{k} space and sum them up in the whole Brillouin zone to represent the time evolution of the entire system.

In this paper, we focus on the HHG spectra driven by a laser pulse (not a continuous wave) with angular frequency Ω because intense laser pulses are usually used in experiments. Hereafter, we simply refer to the angular frequency as frequency unless otherwise noted. In the Coulomb gauge, the vector potential of a laser pulse with frequency Ω is defined as

$$\mathbf{A}(t) = \frac{E_{ac}}{\Omega \sqrt{1 + \epsilon^2}} f_{\text{env}}(t) \begin{pmatrix} \cos(\Omega t) \\ \epsilon \sin(\Omega t) \end{pmatrix}, \quad (5)$$

where E_{ac} is the strength of the AC electric field of the pulse, and $f_{\text{env}}(t)$ is a Gaussian envelope function $f_{\text{env}}(t) = \exp[-2(\ln 2)(t^2/t_{\text{FWHM}}^2)]$ with full width at half-maximum t_{FWHM} . To fix the pulse width, we adopt the five-cycle period of laser at $\Omega = 0.2t_0$ as the standard of t_{FWHM} . The dimensionless parameter for the field strength E_{ac} is given by $eE_{ac}a/t_0$: For graphene, $eE_{ac}a/t_0 = 0.01$ corresponds to $E_{ac} \sim 1.1$ MV/cm. The laser ellipticity ϵ denotes the degree of laser polarization: $\epsilon = 0$ means a linear polarization along the x -axis, while $\epsilon = \pm 1$ denotes a circular one.

To analyze the nonlinear optical response, we consider the electric current in the whole system,

$$\begin{aligned} \hat{\mathbf{J}}(t) &= \frac{\partial \hat{H}(t)}{\partial \mathbf{A}(t)} = \sum_{\mathbf{k}} \sum_{\alpha,\beta} \mathbf{C}_{\alpha,\mathbf{k}}^\dagger \mathcal{J}_{\alpha\beta}[\mathbf{k} + e\mathbf{A}(t)] \mathbf{C}_{\beta,\mathbf{k}} \\ &=: \sum_{\mathbf{k}} \hat{\mathbf{J}}_{\mathbf{k}}(t), \end{aligned} \quad (6)$$

and the expectation value per unit cell, $\mathbf{J}(t) = \frac{1}{N} \sum_{\mathbf{k}} \mathbf{J}_{\mathbf{k}}(t) = \frac{1}{N} \sum_{\mathbf{k}} \langle \hat{\mathbf{J}}_{\mathbf{k}}(t) \rangle_t$, as an observable of interest. Here, N is the system size, $\mathcal{J}_{\alpha\beta}[\mathbf{k} + e\mathbf{A}(t)] = \frac{\partial}{\partial \mathbf{A}} M_{\alpha\beta}[\mathbf{k} + e\mathbf{A}(t)] = \mathbf{j}_{\mathbf{k}+e\mathbf{A}(t)}^x(\sigma_x)_{\alpha\beta} + \mathbf{j}_{\mathbf{k}+e\mathbf{A}(t)}^y(\sigma_y)_{\alpha\beta} + \mathbf{j}_{\mathbf{k}+e\mathbf{A}(t)}^z(\sigma_z)_{\alpha\beta}$ with $(\mathbf{j}_{\mathbf{k}}^x, \mathbf{j}_{\mathbf{k}}^y, \mathbf{j}_{\mathbf{k}}^z) = (et_0 \sum_{\ell=1}^3 \mathbf{d}_\ell \sin(\mathbf{k} \cdot \mathbf{d}_\ell), et_0 \sum_{\ell=1}^3 \mathbf{d}_\ell \cos(\mathbf{k} \cdot \mathbf{d}_\ell), \mathbf{0})$, and $\langle \dots \rangle_t = \text{Tr}[\hat{\rho}(t) \dots]$ denotes the expectation value for a density matrix $\hat{\rho}(t)$. Note that this paper concentrates on laser application to nonequilibrium steady states with a steady current in the graphene model. We are therefore interested in the difference between the electric currents of a laser-irradiated state and the initial steady one. When $\mathbf{J}(t)$ evolves in time, it becomes a source of electromagnetic radiation. The radiation is known to be proportional to

$d\mathbf{J}(t)/dt$ within the dipole radiation approximation, and the normalized radiation power spectrum of high-order harmonics (i.e., HHG spectrum) at frequency ω is given by [77]

$$I_{x,y}(\omega) = |\omega J_{x,y}(\omega)|^2, \quad (7)$$

where $J_x(\omega)$ and $J_y(\omega)$ are the Fourier components of $\mathbf{J}(t) = (J_x(t), J_y(t))$ in the temporal direction [see Fig. 1(b)]. To find characteristic features of the HHG spectra, we will also estimate the power spectrum of the n th-order harmonics, which is defined as

$$\tilde{I}_{x,y}(n\Omega) = \int_{(n-\frac{1}{2})\Omega}^{(n+\frac{1}{2})\Omega} d\omega I_{x,y}(\omega). \quad (8)$$

B. Current-induced steady state

To consider the current-induced steady state, we employ the Boltzmann equation approach [73]. The Boltzmann equation under the application of a static electric field \mathbf{E}_{dc} is given by

$$\frac{\partial f(\mathbf{k}, t)}{\partial t} - e\mathbf{E}_{\text{dc}} \cdot \frac{\partial f(\mathbf{k}, t)}{\partial \mathbf{k}} = \left(\frac{\partial f}{\partial t} \right)_{\text{col}}, \quad (9)$$

where $f(\mathbf{k}, t)$ is a nonequilibrium distribution function for electrons, and $(\frac{\partial f}{\partial t})_{\text{col}}$ is a collision term. Using the relaxation-time approximation and assumption of a system being steady state (i.e., $\frac{\partial f}{\partial t} = 0$), the Boltzmann equation leads to the steady-state distribution function

$$f_{\text{ss}}(\mathbf{k}) = f_0(\mathbf{k}) + e\tau \mathbf{E}_{\text{dc}} \cdot \frac{\partial f_{\text{ss}}(\mathbf{k})}{\partial \mathbf{k}} \approx f_0(\mathbf{k} + \delta_{\text{dc}}), \quad (10)$$

where $f_0(\mathbf{k})$ is the Fermi distribution function $f_0(\mathbf{k}) = (e^{\beta(\epsilon_{\mathbf{k}} - \mu)} + 1)^{-1}$, with β being the inverse temperature, τ denotes the relaxation time of an electron, and $\delta_{\text{dc}} = e\tau \mathbf{E}_{\text{dc}}$. The schematic image of the steady-state distribution is given in Fig. 2(a). Hereafter, we take the zero-temperature limit (i.e., $\beta \rightarrow \infty$) and assume $\delta_{\text{dc}} \parallel \hat{e}_x$ for simplicity.

When we utilize the result of the relaxation-time approximation of Eq. (10), we should be careful about the following two points. The first one is that we have assumed the condition of $\delta_{\text{dc}} a \ll 1$ with $\delta_{\text{dc}} = |\delta_{\text{dc}}|$ in Eq. (10). For graphene, τ is estimated as $\tau \sim 1$ ps [78], and therefore the condition $\delta_{\text{dc}} = |\delta_{\text{dc}}|$ holds if the DC electric field satisfies the inequality $E_{\text{dc}} \ll 10^4$ V/cm. If the DC conductivity of graphene near $\mu = 0$ can be estimated as the universal value $e^2/(4\hbar)$ [75,79], the relation $E_{\text{dc}} \ll 10^4$ V/cm is equivalent to the condition that DC electric current is much smaller than 1 A/cm. In experiments, the maximum value of the observed DC current in monolayer graphene approaches ~ 30 A/cm [80], which is clearly outside the condition of $E_{\text{dc}} \ll 10^4$ V/cm. However, the experimental result indicates that the condition of $E_{\text{dc}} \ll 10^4$ V/cm is easily satisfied by applying a weak DC electric field (i.e., weak voltage) to graphene. We have performed all calculations in this weak-electric-field regime with the relation of Eq. (10), in which the laser response is linearly proportional to the DC field, as we will show in Sec. III A.

The second point is that the Boltzmann equation approach, including Eq. (10), is valid only when the chemical potential is sufficiently far from the Dirac point $\mu = 0$ [62] and a

sufficiently large Fermi surface exists. The Boltzmann equation is a one-band effective theory that contains the intraband dynamics while neglecting the interband one. When the chemical potential is close to the Dirac point or the DC current is strong, the interband transition is not negligible, and the Boltzmann equation approximation breaks down. Therefore, the minimum value $|\mu_0|$ exists when we apply the Boltzmann equation to graphene. The value is given by $|\mu_0| \sim |v_F \delta_{\text{dc}}| \sim ev_F \tau E_{\text{dc}}$. For graphene, it is estimated as $|\mu_0| \sim 0.2$ eV under the application of a DC electric field $E_{\text{dc}} \sim 100$ V/cm.

Figure 2(b) shows the difference between the distribution functions of nonequilibrium steady and equilibrium states,

$$\Delta f(\mathbf{k}) = f_{\text{ss}}(\mathbf{k}) - f_0(\mathbf{k}), \quad (11)$$

at $\delta_{\text{dc}} a = 0.01$, $\mu/t_0 = 0.7$, and $\Delta = 0$ in \mathbf{k} space. This is induced by the application of a DC electric field. The red region shows the DC-field driven change of electron occupation from a valence-band one-particle state to a two-particle one at the subspace with a wave vector \mathbf{k} , while the blue region shows the reverse change at \mathbf{k} , i.e., the change from a two-particle occupied state to a one-particle one. As we will discuss later in Sec. III B, the even-order harmonics are generated only from photoexcitations in the blue area of Fig. 2(b).

C. Time evolution and photoexcitations

When we consider the laser-driven dynamics in graphene, we set the initial state to the current-induced steady state of $f_{\text{ss}}(\mathbf{k})$. In this paper, we compute the time evolution of the density matrix (not the quantum state) to describe such laser-driven dynamics, taking dissipation effects into account.

As we mentioned in Sec. II A, since the time-dependent Hamiltonian has a \mathbf{k} -diagonal form, we can independently solve the time evolution for each wave vector \mathbf{k} under the assumption that dissipation effects at \mathbf{k} and \mathbf{k}' are simply independent of each other. We thereby introduce the \mathbf{k} -decomposed master equation of the GKSL form [48,49,69–72] as the equation of motion

$$\frac{d\hat{\rho}_{\mathbf{k}}(t)}{dt} = -i[\hat{H}_{\mathbf{k}}(t), \hat{\rho}_{\mathbf{k}}(t)] + \gamma \left(\hat{L}_{\mathbf{k}} \hat{\rho}_{\mathbf{k}}(t) \hat{L}_{\mathbf{k}}^\dagger - \frac{1}{2} \{ \hat{L}_{\mathbf{k}}^\dagger \hat{L}_{\mathbf{k}}, \hat{\rho}_{\mathbf{k}}(t) \} \right), \quad (12)$$

where $\hat{\rho}_{\mathbf{k}}(t)$ and $\hat{L}_{\mathbf{k}}$ are the density matrix and the jump operator for the subspace with wave vector \mathbf{k} , respectively. The first and second terms on the right-hand side describe the unitary and dissipative time evolutions, respectively. The phenomenological relaxation rate γ represents the typical relaxation time of system $\tau \sim 1/\gamma$, where we simply neglect the \mathbf{k} dependence of γ in this paper. We set $\gamma = 0.1t_0$, corresponding to $\tau \sim 2.4$ fs. The initial current-induced steady state is described by $\hat{\rho}_{\mathbf{k}}(t_{\text{ini}}) = \hat{\rho}_{\mathbf{k}}^{\text{dc}} = |g_{\mathbf{k}+\delta_{\text{dc}}}\rangle \langle g_{\mathbf{k}+\delta_{\text{dc}}}|$ at the initial time $t = t_{\text{ini}}$. To calculate realistic HHG spectra under the application of DC current, we set the jump operators at each \mathbf{k} to relax to the steady state $f_{\text{ss}}(\mathbf{k})$. To this end, we define the jump operator as $\hat{L}_{\mathbf{k}} = \hat{L}_{\mathbf{k}}^{\text{dc}} = |g_{\mathbf{k}+\delta_{\text{dc}}}\rangle \langle e_{\mathbf{k}+\delta_{\text{dc}}}|$, which induces an interband electron transition from the conduction to the valence band. This jump operator satisfies the detailed balance condition at zero temperature when we consider the

equilibrium limit of $\delta_{\text{dc}} \rightarrow \mathbf{0}$, i.e., the absence of a DC electric field.

We note that the master equation with the above jump operator can be mapped to a so-called optical Bloch equation (see Appendix B). The jump operator induces both longitudinal and transverse relaxation processes in the Bloch-equation picture.

D. Reduction of the density matrix size

Here, we discuss how to combine the steady state of the Boltzmann equation and the master equation in the computation of the density matrix. The main target of the present study is the case with a finite μ , but first we briefly touch on the case of $\mu = 0$ and $\delta_{\text{dc}} = \mathbf{0}$, in which the valence band is completely occupied and the conducting band is empty in the initial state, namely, each subspace with \mathbf{k} has one electron. Since both the graphene's tight-binding Hamiltonian and the light-matter coupling do not change the electron number, it is enough to consider two basis states $|g_{\mathbf{k}}\rangle$ and $|e_{\mathbf{k}}\rangle$ at each \mathbf{k} . Therefore, the density matrix $\hat{\rho}_{\mathbf{k}}(t)$ is given by a 2×2 form.

On the other hand, when we study the case with a Fermi surface and $\mu \neq 0$ in the presence or absence of a DC electric field, the density matrix $\hat{\rho}_{\mathbf{k}}(t)$ seems to be a 4×4 form because two-electron or completely empty states exist in a certain regime of the \mathbf{k} space in addition to the one-electron state. For $\mu > 0$, we have two-electron states, while empty states appear for $\mu < 0$ [see Fig. 2(a)]. A natural set of the bases at each \mathbf{k} is given by $(|0_{\mathbf{k}}\rangle, |g_{\mathbf{k}}\rangle, |e_{\mathbf{k}}\rangle, |2_{\mathbf{k}}\rangle)$, in which $|0_{\mathbf{k}}\rangle$ is the empty state and $|2_{\mathbf{k}}\rangle = \xi_{\mathbf{k}}^{\dagger} \zeta_{\mathbf{k}}^{\dagger} |0_{\mathbf{k}}\rangle$ is the two-electron state. However, the Hamiltonian $\hat{H}_{\mathbf{k}}(t)$, the electric current $\hat{\mathbf{J}}_{\mathbf{k}}(t)$, and the jump operator $\hat{L}_{\mathbf{k}}$ are represented as a 2×2 matrix, namely, $\hat{H}_{\mathbf{k}}(t)|\alpha_{\mathbf{k}}\rangle = \hat{\mathbf{J}}_{\mathbf{k}}(t)|\alpha_{\mathbf{k}}\rangle = \hat{L}_{\mathbf{k}}|\alpha_{\mathbf{k}}\rangle = 0$ with $\alpha = \{0, 2\}$. In other words, there is no unitary dynamics in the subspace of $|0_{\mathbf{k}}\rangle$ and $|2_{\mathbf{k}}\rangle$. In the absence of a DC field, we thus obtain $\mathbf{J}_{\mathbf{k}}(t) = \mathbf{0}$ for the range of $\varepsilon(\mathbf{k}) < |\mu|$, and we can still use the 2×2 -form master equation for $\varepsilon(\mathbf{k}) > |\mu|$. Even if we consider our main target of the case with a finite DC field and a finite wave-vector shift $\mathbf{k} + \delta_{\text{dc}}$, a similar structure still holds. Namely, we can use the 2×2 master equation for one-electron states, while it is not necessary to the time evolution for a subspace of $|0_{\mathbf{k}}\rangle$ and $|2_{\mathbf{k}}\rangle$.

The above discussion can easily be extended to the case of finite temperatures. At finite temperatures, the distribution function of electrons becomes smooth, and the states $|0_{\mathbf{k}}\rangle$ and $|2_{\mathbf{k}}\rangle$ exist with a finite probability. However, there is no unitary dynamics for $|0_{\mathbf{k}}\rangle$ and $|2_{\mathbf{k}}\rangle$, and it is still enough to consider only the two bases $(|g_{\mathbf{k}}\rangle, |e_{\mathbf{k}}\rangle)$. For the relaxation process, we should use the two jump operators

$$\hat{L}_{\mathbf{k}}^{(1)} = |g_{\mathbf{k}+\delta_{\text{dc}}}\rangle\langle e_{\mathbf{k}+\delta_{\text{dc}}}|, \quad (13)$$

$$\hat{L}_{\mathbf{k}}^{(2)} = |e_{\mathbf{k}+\delta_{\text{dc}}}\rangle\langle g_{\mathbf{k}+\delta_{\text{dc}}}|, \quad (14)$$

to meet the detailed balance condition. In the absence of lasers, the system should relax to the equilibrium state after a sufficiently long time. One may hence determine the relaxation rates $\gamma_{\mathbf{k}+\delta_{\text{dc}}}^{(1,2)}$ for $\hat{L}_{\mathbf{k}}^{(1,2)}$ such that they satisfy the detailed balance condition

$$\gamma_{\mathbf{k}+\delta_{\text{dc}}}^{(1)} e^{-\beta E_{\mathbf{k}+\delta_{\text{dc}}}} = \gamma_{\mathbf{k}+\delta_{\text{dc}}}^{(2)} e^{\beta E_{\mathbf{k}+\delta_{\text{dc}}}}. \quad (15)$$

We note that for $\delta_{\text{dc}} = 0$, Eq. (15) makes the system approach a finite-temperature thermal state in the canonical ensemble (not the grand-canonical ensemble). Even in many-electron systems, if we focus on a subspace with a fixed electron number, it is enough to consider the canonical distribution. In fact, as we mentioned, we may concentrate on only one-particle states in the full Hilbert space at each \mathbf{k} to analyze the time evolution of our model.

E. Time evolution of the observable

Within the formalism of the Markovian master equation, the expectation value of the electric current at time t is given by

$$\mathbf{J}(t) = \frac{1}{N} \sum_{\mathbf{k}} \mathbf{J}_{\mathbf{k}}(t) = \frac{1}{N} \sum_{\mathbf{k}} \text{Tr}[\hat{\rho}_{\mathbf{k}}(t) \hat{\mathbf{J}}_{\mathbf{k}}(t)]. \quad (16)$$

In this paper, the computation is always done in \mathbf{k} space, and we take 1280×1280 points in an equally spaced fashion in the full Brillouin zone, which corresponds to the system size $N = 1280 \times 1280$. The current $\mathbf{J}(t)$ can be divided into a contribution of an interband transition and an intraband one as $\mathbf{J}(t) = \mathbf{J}_{\text{inter}}(t) + \mathbf{J}_{\text{intra}}(t)$. The interband (intraband) transition contribution arises from the time evolution of off-diagonal (diagonal) density matrix elements.

F. Advantages of the master equation

Here, we comment on two important aspects of the numerical method we use in the present study. A significant advantage of the use of Eqs. (12) and (16) is that one can directly obtain realistic HHG spectra from their solution without any additional process because the master equation can take an experimentally inevitable dissipation effect. On the other hand, if we solve the standard Schrödinger equation for laser-driven electron systems, an artificial procedure like the use of a ‘‘window function’’ is often necessary to obtain proper HHG spectra. This is because the energy injected by a laser pulse always remains in the system within the Schrödinger equation formalism, and such a setup of an isolated system differs considerably from real experiments.

Another point is that the numerical analysis of the master equation enables us to compute laser ‘‘pulse’’ driven HHG spectra directly. This is in contrast with analytical computation methods of HHG spectra (e.g., linear and nonlinear response theories), in which one usually considers the optical response to an ideal ‘‘continuous wave’’ ($t_{\text{FWHM}} \rightarrow \infty$). Since a finite-width pulse is used in experiments, the ability to directly compute pulse-driven dynamics could be another advantage of the master equation approach.

III. COMPUTATION OF HHG SPECTRA

This section is the main content of the present study. We show several numerical results and the essential properties of HHG spectra, especially even-order harmonics.

A. HHG spectra and DC-electric-field dependence

First, we focus on the typical HHG spectra and the DC-electric-field dependence of HHG in graphene. Figure 3 shows

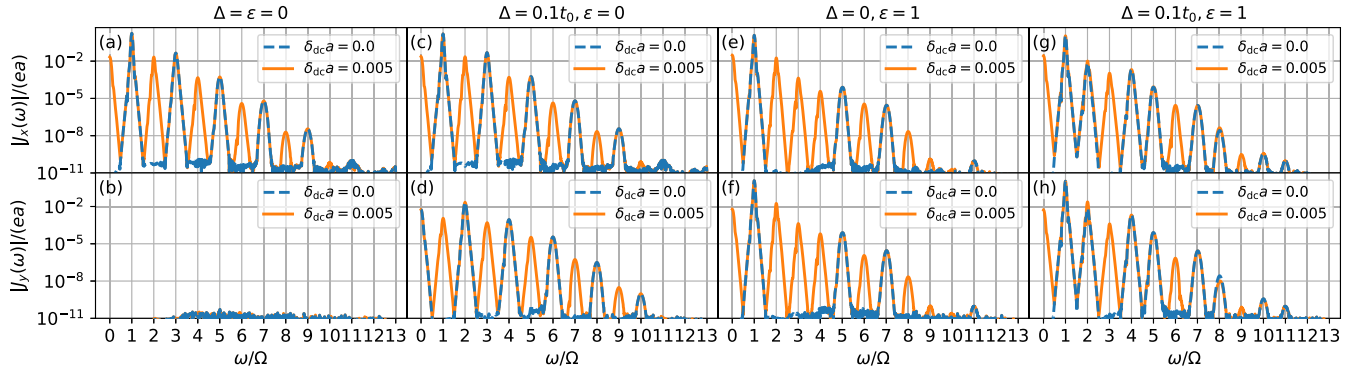


FIG. 3. Laser-pulse driven HHG spectra of the current along the (x, y) -directions in graphene models with/without DC electric field E_{dc} at $\mu = 0.4t_0 = \Omega$. (a)–(h) Comparative plots of $|J_x(\omega)|$ (top row) and $|J_y(\omega)|$ (bottom row) at $\delta_{dc}a = 0$ and 0.005 for different conditions of the staggered potential Δ and the laser ellipticity ϵ . Panels (a) and (b) show data for $(\Delta, \epsilon) = (0, 0)$, (c) and (d) are for $(\Delta, \epsilon) = (0.1t_0, 0)$, (e) and (f) are for $(\Delta, \epsilon) = (0, 1)$, and (g) and (h) are for $(\Delta, \epsilon) = (0.1t_0, 1)$. Other parameters are $eE_{ac}a/t_0 = 0.05$, $\gamma = 0.1t_0$, and $\Delta = 0$.

typical HHG spectra of the current along the x and y directions $|J_{x,y}(\omega)|$ with or without DC current ($\delta_{dc}a = 0$ and 0.005). The laser intensity is chosen to be moderate ($eE_{ac}a/t_0 = 0.005$), and the frequency is equal to the chemical potential ($\Omega = \mu$). Different panels correspond to different values of the staggered potential Δ and the laser ellipticity ϵ . Figure 3 shows that $2n$ th- or $3n$ th-order harmonics ($n \in \mathbb{Z}$) are forbidden in the absence of DC current, depending on the existence or absence of Δ and ϵ , except for the panel (b). It also shows that a weak DC current with $\delta_{dc}a = 0.005$, which breaks the inversion symmetry, is enough to obtain $2n$ th- or $3n$ th-order harmonics, whose intensity is comparable with that of neighboring $(2n + 1)$ th- or $(3n + 1)$ th-order harmonics.

These features, i.e., the appearance or absence of n th-order harmonics, can be understood by finding a dynamical symmetry [48,49,52,81–84] of the system. The dynamical symmetry is a sort of symmetry including a time translation as well as a usual symmetry operation in time-periodic systems like the present system-laser complex (see Appendix A). It is defined by the following relation:

$$\hat{U}^\dagger \hat{H}(t + \Delta t) \hat{U} = \hat{H}(t), \quad (17)$$

where $\hat{H}(t) = \hat{H}(t + T)$ is the time-periodic Hamiltonian of the target system with a time period T , Δt ($0 < \Delta t < T$) is a time shift, and \hat{U} is a unitary (or antiunitary) operator. In laser-driven systems, Ω is the laser frequency and $T = 2\pi/\Omega$ is the period of the laser. For such a dynamical symmetric system, if a vector operator $\hat{\mathcal{O}}(t) = (\hat{\mathcal{O}}_1(t), \hat{\mathcal{O}}_2(t), \dots)$ satisfies a similar relation

$$\hat{U}^\dagger \hat{\mathcal{O}}(t + \Delta t) \hat{U} = \mathcal{R} \hat{\mathcal{O}}(t), \quad (18)$$

then we can lead to a selection rule of $\mathcal{O}(m\Omega) = 0$ with a certain integer m . Here, \mathcal{R} is a matrix acting only on the vector $\hat{\mathcal{O}}$, and the vector $\mathcal{O}(\omega)$ is the Fourier transform of the expectation value $(\hat{\mathcal{O}}(t))_t$ along the time direction. In the above symmetry argument, we have assumed that $\hat{U}^\dagger \hat{\rho}(t + \Delta t) \hat{U} = \hat{\rho}(t)$ holds, namely, not only the Hamiltonian but also the density matrix (quantum states) is dynamical symmetric [48,49,83,84]. When we consider HHG spectra, the operator $\hat{\mathcal{O}}(t)$ should be chosen to the current $\hat{\mathcal{J}}(t)$. For instance, if a system has a dynamical symmetry with $\Delta t = T/2$ and the

current satisfies $\hat{U}^\dagger \hat{\mathcal{J}}_\alpha(t + \Delta t) \hat{U} = -\hat{\mathcal{J}}_\alpha(t)$ ($\alpha = x$ or y), one can prove that $J_\alpha(2n\Omega) = 0$ with arbitrary integer n , i.e., even-order harmonics all vanish.

Table I summarizes dynamical symmetries and the resulting selection rules that hold for some panels of Fig. 3 in the absence of an extrinsic DC current. The pair $(\hat{U}, t + \Delta t)$ represents the symmetry operation and the time translation of dynamical symmetry we consider. An operation without time translation, i.e., (\hat{U}, t) , corresponds to a standard static symmetry. In the case of $\Delta = 0$ and linear polarization ($\epsilon = 0$) as in Figs. 3(a) and 3(b), the dynamical symmetry $(\hat{U}_{\sigma_{yz}}, t + T/2)$ prohibits even-order harmonics of $J_x(2n\Omega)$ (see Appendix A). Here, $\hat{U}_{\sigma_{yz}}$ and $\hat{U}_{\sigma_{zx}}$ are, respectively, the mirror operations across the y - z plane ($x \rightarrow -x$) and the z - x plane ($y \rightarrow -y$). In addition to this dynamical symmetry, the system possesses the (static) mirror symmetry of $\hat{U}_{\sigma_{zx}}$. From these dynamical and static symmetries, optical responses in the y direction are all shown to be prohibited. A finite $\Delta \neq 0$ breaks a dynamical symmetry with in-plane C_2 rotation, $(\hat{U}_2, t + T/2)$, allowing even-order harmonics in the y direction as shown in Fig. 3(d). On the other hand, $(\hat{U}_{\sigma_{yz}}, t + T/2)$ is preserved regardless of the value of Δ , and as a result, even-order harmonics in the x direction are all suppressed even if Δ exists [see Figs. 3(a) and 3(c)].

In the case of circular polarization ($\epsilon = 1$), we should note the following two dynamical symmetries: (i) $(\hat{U}_2, t + T/2)$ and (ii) $(\hat{U}_3, t + T/3)$, where \hat{U}_3 is the in-plane C_3 rotation. For $\Delta = 0$, both (i) and (ii) hold, and they prohibit even-order and $3n$ th-order harmonics in both x and y directions ($n \in \mathbb{Z}$). On the other hand, for $\Delta \neq 0$, (i) is violated, and only $3n$ th-order harmonics are prohibited.

The application of a DC current breaks all these dynamical symmetries, allowing the appearance of all the harmonics. However, the static mirror symmetry $\hat{U}_{\sigma_{zx}}$ is not broken by the DC current in the x direction, and therefore the response in the y direction is suppressed.

These clear properties of HHG spectra are consistent with our numerical results of Fig. 3. We emphasize that several HHG signals can be activated and controlled by an external DC current, as shown in Fig. 3. Hereafter, we mainly focus on the linear polarized light of $\epsilon = 0$, which has often been used in experiments.

TABLE I. Various selection rules for HHG in the graphene model of Eq. (3) without DC current. These rules are derived from the (dynamical) symmetries. Each pair $(\hat{U}, t + \Delta t)$ represents the static symmetry operation and the time translation $t \rightarrow t + \Delta t$ of a dynamical symmetry. We list four cases [(i)–(iv)] of $\Delta = 0$ (e.g., graphene) and $\Delta \neq 0$ (e.g., transition-metal dichalcogenides; TMDC) with linear polarized light (LPL) along the x direction or circularly polarized light (CPL). These dynamical symmetries are all broken by the application of DC current, except for $\hat{U}_{\sigma_{2x}}$.

	(i) LPL $\parallel \hat{e}_x, \Delta = 0$	(ii) LPL $\parallel \hat{e}_x, \Delta \neq 0$	(iii) CPL, $\Delta = 0$	(iv) CPL, $\Delta \neq 0$
(Dynamical) symmetry	$(\hat{U}_{\sigma_{yz}}, t + T/2)$ $(\hat{U}_2, t + T/2)$ $(\hat{U}_{\sigma_{2x}}, t)$	$(\hat{U}_{\sigma_{yz}}, t + T/2)$	$(\hat{U}_2, t + T/2)$ $(\hat{U}_3, t + T/3)$	$(\hat{U}_3, t + T/3)$
Selection rule ($n \in \mathbb{Z}$)	$J_x(2n\Omega) = 0$ $J_y(t) = 0$	$J_x(2n\Omega) = 0$ $J_y((2n+1)\Omega) = 0$	$J(2n\Omega) = 0$ $J(3n\Omega) = 0$	$J(3n\Omega) = 0$

Before ending this subsection, we remark on two things. First, as we discussed in Sec. II B, the current-induced steady state obtained by the Boltzmann equation is valid only when the current (or DC electric field) is sufficiently small, i.e., $\delta_{dc}a \ll 1$. In this condition, the intensities of DC-field-induced harmonics are expected to be proportional to the DC-field power E_{dc}^2 because the DC-field-induced current $J_\alpha(\omega)$ would linearly respond to E_{dc} . Figures 4(a) and 4(b) show that intensities of the DC-field-induced second- and fourth-order harmonic generations (SHG and FHG) are both almost proportional to E_{dc}^2 in a moderate- E_{dc} region. In a sufficiently weak-field regime of $\delta_{dc}a \lesssim 10^{-3}$, they deviate from the E_{dc}^2 curves. This is because a small E_{dc} causes a very small $\Delta f(\mathbf{k})$, and the accurate numerical detection of the effects of such a small $\Delta f(\mathbf{k})$ is beyond our resolution in \mathbf{k} space ($N = 1280 \times 1280$). On the other hand, in the strong E_{dc} regime, SHG and FHG intensities again deviate from the E_{dc}^2 line since their nonlinear E_{dc} dependence is activated. We therefore focus on the mid E_{dc} region and set $\delta_{dc}a = 0.005$ in the following sections unless otherwise noted.

The second point concerns the time periodicity in the above argument of dynamical symmetry. When we argue the dynamical symmetry, we usually assume that the Hamiltonian satisfies $\hat{H}(t) = \hat{H}(t + T)$. Namely, we implicitly consider a system irradiated by a ‘‘continuous wave.’’ On the other hand, a short laser pulse is generally used in experiments. Therefore, the argument based on dynamical symmetry does

not seem to be applicable to discussing pulse-induced HHG spectra. However, empirically, selection rules based on dynamical symmetry work at least at a qualitative level, even if the applied laser pulse contains only a few cycles. As we discussed above, our results on laser pulses in Fig. 3 are indeed explained by dynamical symmetries in Table I.

B. Laser-frequency dependence

Next, we show a laser-frequency dependence of HHG spectra, especially SHG, FHG, and sixth-order harmonic generation (sixth HG). We show the characteristic resonance structure and how the frequency dependence changes with the growth of laser strength.

Figures 5(a) and 5(b), respectively, show the laser-frequency Ω dependence of the SHG intensities $\tilde{I}_x(2\Omega)$ for different chemical potentials μ in the application of weak and strong laser pulses [$eE_{ac}a/t_0 = (0.001, 0.1)$]. In the weak pulse case of Fig. 5(a), we find a peak of SHG at $\Omega = \mu$, and its intensity is proportional to Ω^{-2} as in Fig. 5(d). These results are consistent with the previous predictions based on the analytical perturbation theory for a Dirac electron model [61], which is valid in a weak AC-field limit. The divergent Ω^{-2} behavior in the low-frequency regime is due to the singular Berry connection of the Dirac cone [61]. Figure 5(c) and the green dashed line in Fig. 5(d) are the analytical results, which correspond, respectively, to Fig. 5(a) and the blue circles in Fig. 5(d). We note that in a large- Ω regime of Fig. 5(d), the SHG peak intensity deviates from the Ω^{-2} line. This is because higher-energy photoexcited electrons, which cannot be described by the \mathbf{k} -linear Dirac electron model, become dominant in the large- Ω regime. The perturbation theory also predicts $J(2\Omega) \propto E_{dc}E_{ac}^2$, and we confirm that this power-law relation holds in our numerical result in the weak laser case of $eE_{ac}a/t_0 = 0.001$ (see Sec. III C). From these results, we can conclude that our numerical method well reproduces the previous analytical predictions.

In the strong laser case of Fig. 5(b), on the other hand, different features of SHG spectra are observed. We again find a peak structure around $\Omega = \mu$, but its intensity is no longer proportional to Ω^{-2} and it clearly increases with growing Ω . Figure 5(d) shows that there are two scaling regimes of the SHG peak intensity: It is proportional to Ω^5 (i.e., non-divergent) in the low- Ω regime, whereas it is proportional to Ω in the high- Ω regime. These scaling laws $\tilde{I}_x(2\Omega) \propto \Omega^5$ and $\propto \Omega^1$ are both nontrivial, and we cannot find any simple

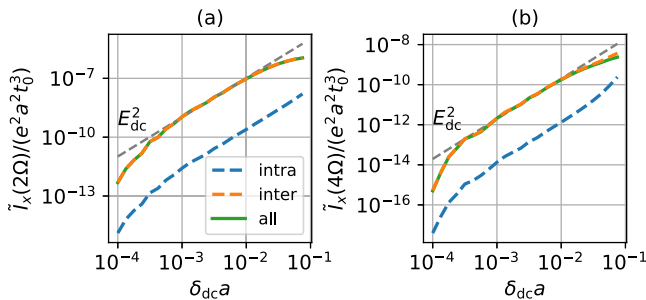


FIG. 4. E_{dc} dependence of (a) SHG [$\tilde{I}_x(2\Omega)$] and (b) FHG [$\tilde{I}_x(4\Omega)$] spectra in pulse-driven graphene at $\mu = \Omega = 0.4t_0$ and $\mu = \Omega/2 = 0.4t_0$. Each graph simultaneously displays the intraband dynamics component (blue line), the interband dynamics component (orange line), and the total spectra (green line). The gray dashed line is the fitting line of the spectra $\propto E_{dc}^2$. The other parameters are set to $eE_{ac}a/t_0 = 0.01$, $\gamma = 0.1t_0$, and $\Delta = \epsilon = 0$.

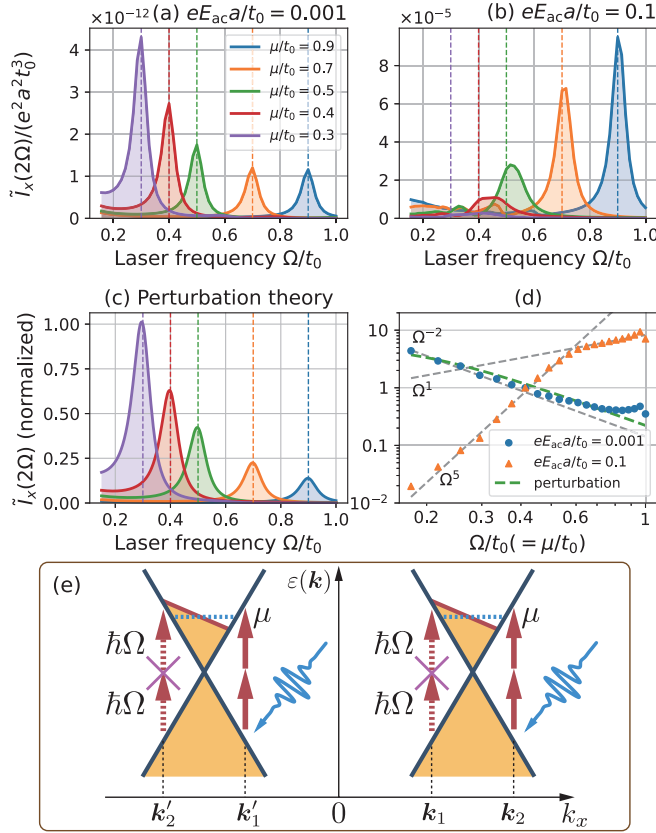


FIG. 5. (a),(b) Ω dependence of SHG [$\tilde{I}_x(2\Omega)$] spectra of the current along the x direction in graphene with DC current at various conditions of chemical potentials $\mu/t_0 = \{0.3, 0.4, 0.5, 0.7, 0.9\}$ under the irradiation of a weak laser (a) ($eE_{ac}a/t_0 = 0.001$) and a strong laser (b) ($eE_{ac}a/t_0 = 0.1$). The dashed lines show the positions of $\Omega = \mu$. (c) DC-current driven SHG spectra computed by second-order perturbation theory in Ref. [61]. Parameters are the same as those of panel (b). (d) Scaling behavior of the SHG peak intensities as a function of Ω . The points are numerically calculated for the cases of weak (blue points) and strong (orange points) lasers. The dashed line shows the result of the perturbation theory. (e) \mathbf{k} -space image of SHG photoexcitations in DC-current driven graphene with $\mathbf{E}_{dc} \parallel \hat{e}_x$ on $k_y = 0$. Red arrows show the two-photon absorption processes, where the laser frequency is chosen to be $\Omega = \mu$, and we temporally revive \hbar . The symbol \times indicates the impossibility of the absorption process. The contribution from the wave-vector pairs \mathbf{k} and \mathbf{k}' , which should cancel each other in inversion-symmetric graphene, becomes finite due to the DC-current driven shift of the Fermi distribution, and it activates even-order harmonics. The other parameters are set to $\delta_{dc}a = 0.005$, $\gamma = 0.1t_0$, and $\Delta = \epsilon = 0$.

explanation for them. We stress that these properties in the nonperturbative, strong-laser regime were first captured by the present numerical method based on the master equation.

Let us consider these resonancelike structures in Fig. 5 from a microscopic viewpoint. Even-order optical responses are generally prohibited in spatial-inversion symmetric electron systems, whereas (as mentioned in Sec. II B) a weak DC electric field (i.e., a weak DC current) causes a shift of the electron distribution and breaks the inversion symmetry. We can prove that in C_2 rotation-symmetric systems, the even-order harmonics generated by electrons in the k_x and $-k_x$

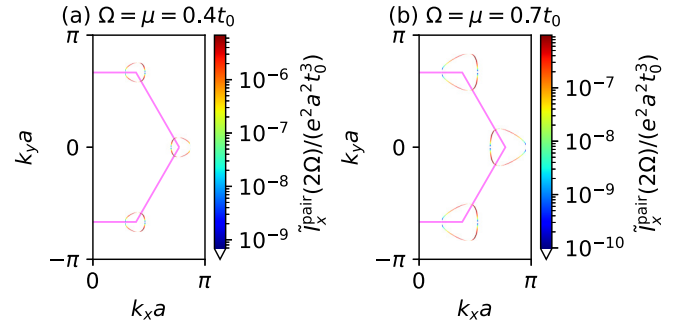


FIG. 6. Numerically computed symmetrical pair of \mathbf{k} -resolved SHG intensity $\tilde{I}_x^{\text{pair}}(\mathbf{k}, 2\Omega)$ of Eq. (20) at (a) $\mu = \Omega = 0.4t_0$ and (b) $\mu = \Omega = 0.7t_0$. The region of a finite $\tilde{I}_x^{\text{pair}}(\mathbf{k}, 2\Omega)$ coincides with that of a finite deviation $\Delta f_{ss}(\mathbf{k})$ in Fig. 2(b). Parameters are set to $eE_{ac}a/t_0 = 0.001$, $\delta_{dc}a = 0.01$, $\gamma = 0.1t_0$, and $\Delta = \epsilon = 0$.

points cancel each other out, and as a result, even-order ones all vanish (see Appendix A 2). When a DC electric field \mathbf{E}_{dc} is applied along the x axis in graphene, the electron distribution changes from a usual distribution with a Fermi surface to an asymmetric one, as shown in Fig. 5(e). For such a shifted distribution of Fig. 5(e), we have one-electron states around $\mathbf{k} = (k_x, k_y)$, while we have two-electron states around $\mathbf{k}' = (-k_x, k_y)$. Therefore, when we tune the laser frequency to $\Omega \sim \mu$, two-photon absorption can take place around \mathbf{k} , whereas it cannot around \mathbf{k}' , as shown in Fig. 5(e). As a result, the cancellation between k_x and $-k_x$ is broken and the SHG peak appears at $\Omega \sim \mu$. This scenario is easily extended to the cases of generic $2n$ th-order HHG in DC-current-driven steady states. In this way, the $2n$ th-order HHG spectra of DC-current-driven graphene are predicted to have a peak when the laser frequency satisfies the following inequality:

$$\mu/n - v_F \delta_{dc}/(2n) \leq \Omega \leq \mu/n + v_F \delta_{dc}/(2n). \quad (19)$$

To see the validity of the above argument about even-order HHG, we define the following \mathbf{k} -resolved SHG intensity:

$$\tilde{I}_x^{\text{pair}}(\mathbf{k}, 2\Omega) = \int_{(2-\frac{1}{2})\Omega}^{(2+\frac{1}{2})\Omega} d\omega |\omega [J_{x,\mathbf{k}}(\omega) + J_{x,\mathbf{k}'}(\omega)]|^2, \quad (20)$$

where $\mathbf{k} = (k_x, k_y)$, $\mathbf{k}' = (-k_x, k_y)$, and this value is defined in half of the Brillouin zone ($k_x > 0$). If the \mathbf{k} - and \mathbf{k}' -point SHG intensities perfectly cancel each other out, the value of $\tilde{I}_x^{\text{pair}}(\mathbf{k}, 2\Omega)$ becomes zero. However, it has a finite value when the cancellation is broken. That is, Eq. (20) can detect the degree of breakdown of the cancellation between \mathbf{k} and \mathbf{k}' points. Figure 6 gives the numerically computed results of $\tilde{I}_x^{\text{pair}}(\mathbf{k}, 2\Omega)$ in half of the Brillouin zone ($k_x > 0$) at $\Omega = \mu$. It shows that $\tilde{I}_x^{\text{pair}}(\mathbf{k}, 2\Omega)$ takes a finite value around \mathbf{K} and \mathbf{K}' Dirac points. Especially, comparing Fig. 6(b) with Fig. 2(b), one sees that $\tilde{I}_x^{\text{pair}}(\mathbf{k}, 2\Omega)$ is enhanced in the region where the electron distribution is shifted [i.e., $\Delta f_{ss}(\mathbf{k}) \neq 0$]. We thus conclude that the argument in the above paragraph is indeed correct.

We further discuss the higher even-order harmonics (FHG and sixth-order HG) in graphene under the application of DC current. As we will soon see, in these harmonics, multiple resonance peaks appear, and the response driven by not only

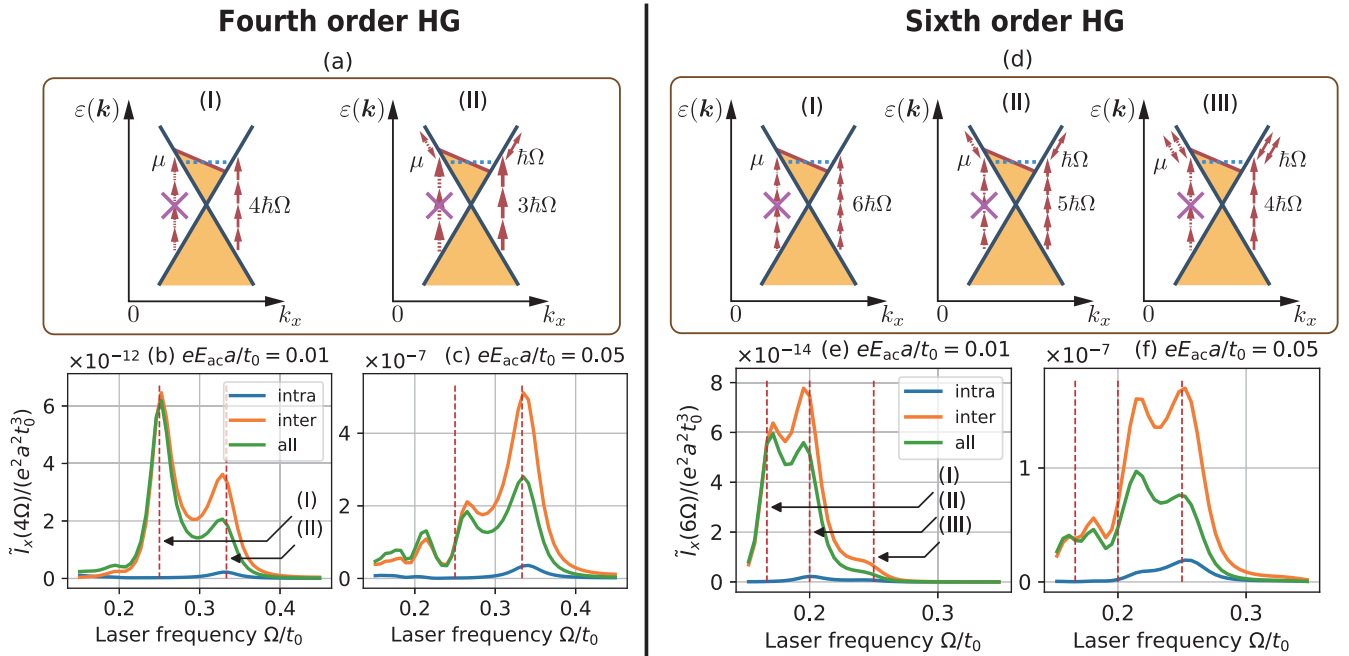


FIG. 7. Laser-frequency Ω dependence of even-order harmonics intensities (bottom row) and schematic images of the photon absorption processes and intraband dynamics corresponding to the bottom row (top row). Each graph in the bottom row simultaneously displays the intraband dynamics intensity (blue line), the interband dynamics one (orange line), and the total one (green line) at $eE_{ac}a/t_0 = 0.01$ and 0.05 . Left panels (a)–(c) represent FHG, and right panels (d)–(f) represent sixth-order HG. In cartoons (a) and (d), we have revived the symbol \hbar . Other parameters are set as follows: $\mu = 0.5t_0$, $\delta_{dc}a = 0.005$, $\gamma = 0.1t_0$, and $\Delta = \epsilon = 0$.

interband but also intraband dynamics becomes dominant for a strong laser pulse.

Figure 7 shows the results of FHG spectra [panels (a)–(c)] and sixth-order HG spectra [panels (d)–(f)] for weak and strong laser pulses. In panels (b), (c), (e), and (f), orange (blue) lines show the contributions from interband (intraband) dynamics, and green lines show the full responses of interband and intraband dynamics as a function of the laser frequency Ω . One sees many peaks in the FHG and sixth-order HG spectra of panels (b), (c), (e), and (f). Among them, the FHG peak at $\Omega = \mu/2$ [(I) in panel (b)] and the sixth-order HG one at $\Omega = \mu/3$ [(I) in panel (e)] can be understood by the perturbation theory: the former and latter correspond, respectively, to four- and six-photon absorption processes, described in the cartoons (I) of Figs. 7(a) and 7(d). In the strong pulse cases corresponding to panels (c) and (f), other peaks become grown at $\Omega = 2\mu/3$ for the FHG and at $\Omega = 2\mu/5$ and $\mu/2$ for the sixth-order HG. For instance, the additional peak of FHG at $\Omega = 2\mu/3$ can be governed by the four-photon process with an interband three-photon absorption and an intraband one-photon dynamics, as shown in the process (II) of Fig. 7(a). In fact, we can observe an enhancement of intraband contribution at $\Omega = 2\mu/3$ with laser intensity increasing, by comparing Figs. 7(b) and 7(c). Hereafter, we refer to a photoexcited process with interband m -photon absorption and intraband n -photon dynamics as an “ $m + n$ process.” For the sixth-order HG, the peaks of $\Omega = 2\mu/5$ and $\Omega = \mu/2$ correspond to the $5 + 1$ process [process (II) of Fig. 7(d)] and the $4 + 2$ process [process (III) of Fig. 7(d)], respectively. We stress that these additional peaks in FHG and sixth-order HG are stronger than the typical perturbative peaks when the laser intensity is large enough ($eE_{ac}a/t_0 = 0.05$).

At the end of this subsection, we briefly compare our numerical method with the analytic perturbation theory. As discussed in Ref. [85], the perturbative calculations make it possible to classify several laser-driven optical processes in a clear, analytic manner. On the other hand, as we explained in this subsection, our numerical analysis classifies different laser-driven processes from the computed spectral peaks of the density matrix and physical quantities, and hence it is generally difficult to classify the optical processes in more detail than the perturbation theory, especially when both interband and intraband processes are intertwined. However, our numerical approach has some advantages: The classification based on perturbative analytical approaches is limited to lower-order perturbation terms, whereas our numerical analysis can capture higher-order nonperturbative contributions. Therefore, these two strategies are complementary to each other. In the present study, we utilize the numerical method based on the GKSL equation to describe the overall characteristics of the spectrum, including higher-order harmonics.

C. Laser-intensity dependence

Next, we show a laser-intensity dependence of HHG spectra, focusing on SHG $\tilde{I}_x(2\Omega)$ and FHG $\tilde{I}_x(4\Omega)$, which appear only when DC current is applied. Figure 8(a) shows the laser-intensity E_{ac} dependence of $\tilde{I}_x(2\Omega)$ for different chemical potential μ under the condition of $\Omega = \mu$, in which the $2 + 0$ process is dominant as in Fig. 2(a). The SHG spectra are proportional to E_{ac}^4 for every μ for a weak enough laser pulse $eE_{ac}a/t_0 \lesssim 10^{-2}$. This feature is consistent with the second-order perturbation theory [61,62]. However, when the laser pulse becomes strong, the SHG intensity is

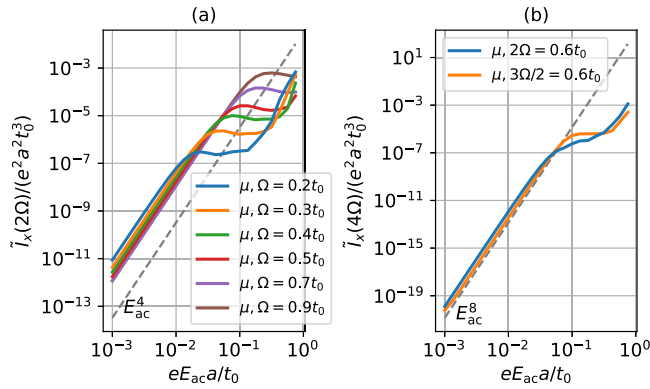


FIG. 8. The E_{ac} dependence of (a) second-order harmonic generation (SHG) [$\tilde{I}_x(2\Omega)$] and (b) fourth-order harmonic generation (FHG) [$\tilde{I}_x(4\Omega)$] spectra in pulse-driven graphene. The gray dashed line represents the fitted line as a guide to the eye: the line of panel (a) is $\propto E_{ac}^4$ and that of (b) is $\propto E_{ac}^8$. (a) SHG spectra at different values of chemical potentials $\mu/t_0 = \{0.2, 0.3, 0.4, 0.5, 0.7, 0.9\}$ under the condition of the laser frequency $\Omega = \mu$. (b) FHG at $\mu = \{2\Omega, 3\Omega/2\} = 0.6t_0$. The other parameters are set as follows: $\delta_{dca} = 0.005$, $\gamma = 0.1t_0$, and $\Delta = \epsilon = 0$.

no longer proportional to E_{ac}^4 , indicating the appearance of the nonperturbative region. Furthermore, we can find that the laser intensity of the crossover from the perturbative to the nonperturbative regime is dependent on the chemical potential μ and laser frequency $\Omega = \mu$. The laser intensity for the crossover is smaller with μ (and laser frequency Ω) decreasing. The laser-intensity dependence of the SHG spectra is consistent with the result of Figs. 5(a) and 5(b).

Figure 8(a) also indicates that the Ω and E_{ac} dependences of $\tilde{I}_x(2\Omega)$ are complicated and correlated in the nonperturbative regime of $eE_{ac}a/t_0 \gtrsim 10^{-1}$. For instance, in Figs. 5(b) and 5(d), we have observed the monotonically increasing Ω dependence for an intense laser $eE_{ac}a/t_0 = 10^{-1}$, but Fig. 8(a) tells us that the Ω dependence further changes if we consider a more intense laser such as $eE_{ac}a/t_0 = 10^0$.

The FHG spectra exhibit a similar feature to that shown in Fig. 8(b). Panel (b) shows the laser-intensity E_{ac} dependence of $\tilde{I}_x(4\Omega)$ for the condition of (I) $\Omega = \mu/2$ and (II) $\Omega = 2\mu/3$, which corresponds to the processes (I) and (II) of Fig. 7(a), respectively. In the weak laser pulse regime $eE_{ac}a/t_0 \lesssim 10^{-2}$, the FHG intensities are proportional to E_{ac}^8 , which is consistent with the fourth-order perturbation viewpoint. We also observe that the perturbative-nonperturbative crossover for condition (II) takes place at a higher laser intensity than for condition (I). This feature explains the peak heights at $\Omega = \mu/2$ and $\Omega = 2\mu/3$ in Figs. 7(b) and 7(c).

D. Effect of a finite mass gap

We have mainly focused on the graphene model with zero staggered potential $\Delta = 0$ so far. This subsection is devoted to a discussion on the effects of a staggered potential Δ under the application of a DC current. Note that a finite Δ induces a mass gap at Dirac points \mathbf{K} and \mathbf{K}' , and we focus on the situation with a Fermi surface, i.e., the chemical potential is significantly larger than the mass gap. In this subsection, we fix

$(\mu, \Delta) = (0.4t_0, 0.1t_0)$ and then mainly see the Ω dependence of the HHG. As we discussed in Sec. III A, when the electric field of linear polarized light is along the x axis, the presence or absence of Δ affects the laser-driven current along the y direction, especially the even-order harmonics. Applying a DC current further induces odd-order harmonics of the current along the y axis. We therefore investigate the behavior of the fundamental frequency response (i.e., the first-order harmonics) $\tilde{I}_y(\Omega)$ among the DC-current driven odd-order harmonics.

Figures 9(b) and 9(c), respectively, show the Ω dependence of $\tilde{I}_y(\Omega)$ induced by weak and strong laser pulses. The orange (blue) line shows the contribution from the interband transition (intraband dynamics), and the green line shows overall intensities. In Fig. 9(b), there is a sharp peak of $\tilde{I}_y(\Omega)$ at $\Omega = 2\mu$ for a weak pulse. This peak is explained by the perturbation argument, in which a one-photon absorption as in the process (I) of Fig. 9(a) is dominant. For a strong laser pulse, additional peaks emerge around $\Omega = \mu$, $\Omega = 2\mu/3$, $\Omega = \mu/2$, etc., as shown in Fig. 9(c). These peak structures can be understood by the nonlinear optical responses, such as two-photon absorption, three-photon absorption, and others, whose images are given in processes (II) and (III) of Fig. 9(a). Figures 9(d) and 9(e) show that these interband transition (photon absorption) processes for $\tilde{I}_y(\Omega)$ accompany the intraband dynamics for $\tilde{I}_x(\Omega)$. Two panels (d) and (e) represent the difference $\Delta\tilde{I}_x(\Omega)$ between $\tilde{I}_x(\Omega)$ under a finite DC current and that under zero DC current. Since the first-order response $\tilde{I}_x(\Omega)$ of the x -direction current exists even in the case without DC current, we introduce $\Delta\tilde{I}_x(\Omega)$. Figure 9(d) shows that for a weak laser pulse, a single peak of $\Delta\tilde{I}_x(\Omega)$ appears around $\Omega = 2\mu$ like $\tilde{I}_y(\Omega)$ of Fig. 9(b). On the other hand, Fig. 9(e) tells us that when the laser pulse becomes strong, multiple peaks of $\Delta\tilde{I}_x(\Omega)$ appear, corresponding to those of $\tilde{I}_y(\Omega)$ in panel (c), and the contributions of not only interband but also intraband dynamics increase in $\Delta\tilde{I}_x(\Omega)$. These results indicate that in the strong-laser regime, $\tilde{I}_y(\Omega)$ exhibits a complex Ω dependence accompanied by the intraband dynamics of $\tilde{I}_x(\Omega)$.

Figure 9(f) represents the laser intensity dependence of $\tilde{I}_y(\Omega)$ at peak positions corresponding to conditions (I), (II), and (III) of panels (a) and (c). Considering the laser frequency values at these peak positions and the fact that the intraband contribution of $\tilde{I}_y(\Omega)$ vanishes in panels (b) and (c), we can predict that the peaks (I), (II), and (III) are viewed, respectively, as linear, third-order, and fifth-order nonlinear optical responses. Namely, their intensities $\tilde{I}_y(\Omega)$ are expected to be proportional to E_{ac}^2 , E_{ac}^6 , and E_{ac}^{10} [remember that $\tilde{I}_y(\Omega) \propto |J_y(\Omega)|^2$]. Figure 9(f) indeed shows that the intensities of $\tilde{I}_y(\Omega)$ at conditions (I), (II), and (III) follow the expected power laws in the region of the weak laser pulse. Therefore, our predictions about the perturbative picture of each peak (I), (II), and (III) are consistent with the numerical results for the weak-laser regime. Moreover, Fig. 9(f) illustrates the crossover from the perturbative to the nonperturbative regimes, demonstrating that our numerical method can capture a broad range from weak to strong lasers.

E. Extremely strong laser fields

In this final subsection, we focus on the case of extremely strong laser fields. We show the HHG spectra $|J_x(\omega)|$ at

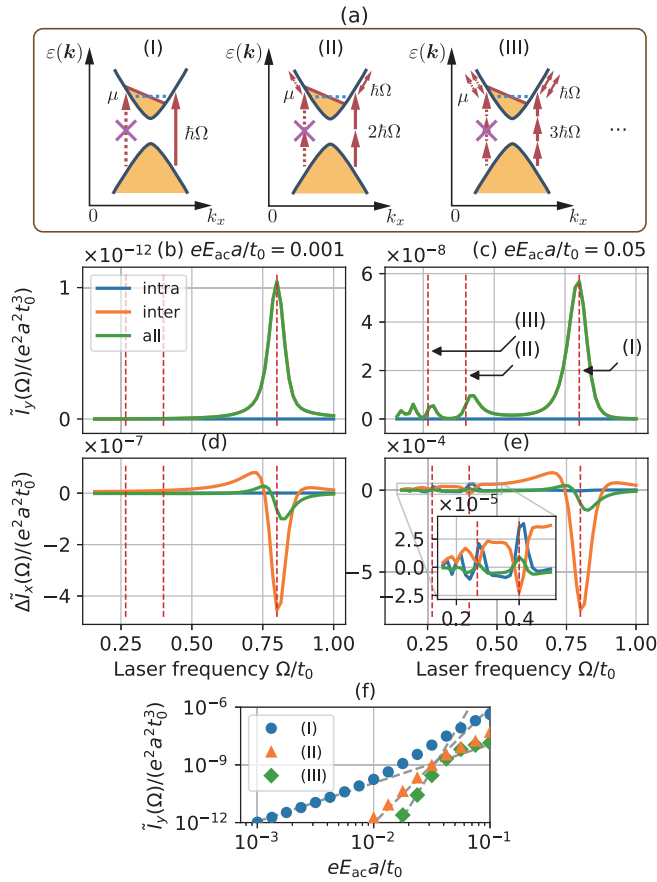


FIG. 9. Several properties of linearly polarized light driven $\tilde{I}_y(\Omega)$ in the gapped graphene model with a finite Δ under the application of a DC current. Directions of both the DC current and the electric field of the laser are parallel to the x axis. (a) Schematic images of the one-photon absorption process (I) and multiphoton processes (II) and (III) with both interband and intraband dynamics in $\tilde{I}_{x,y}(\Omega)$. In the panels, we have revived the symbol \hbar . (b),(c) The Ω dependence of $\tilde{I}_y(\Omega)$ spectra in gapped graphene model at chemical potential $\mu/t_0 = 0.4$ under the irradiation of (b) a weak laser pulse with $eE_{ac}a/t_0 = 0.001$ and (c) a strong one with $eE_{ac}a/t_0 = 0.05$. (d),(e) The difference $\Delta \tilde{I}_x(\Omega)$ between $\tilde{I}_x(\Omega)$ under the condition of a finite DC current ($\delta_{dc}a = 0.005$) and that under zero DC current ($\delta_{dc}a = 0$). Panel (d) is the result of a weak laser pulse, while panel (e) is a strong pulse. (f) The E_{ac} dependence of the peak intensities of $\tilde{I}_y(\Omega)$ in the gapped graphene model. Blue (I), orange (II), and green (III) points, respectively, correspond to the peaks at positions (I), (II), and (III) of panel (c). Fitting dashed lines are a guide for the eye: lines for the conditions (I), (II), and (III), respectively, are proportional to E_{ac}^2 , E_{ac}^6 , and E_{ac}^{10} . Due to the limitations of the accuracy of the numerical computation, intensities below 10^{-12} are not displayed. Other parameters are $\gamma = 0.1t_0$, $\Delta = 0.1t_0$, and $\epsilon = 0$.

$\delta_{dc}a = 0$ and 0.005 under the irradiation of the strong laser pulses $eE_{ac}a/t_0 = (0.1, 0.3, 0.5)$ in Figs. 10(a)–10(c). The effect of DC current clearly appears in Fig. 10(a), which is shown as an activation of the even-order harmonics at $E_{dc} \neq 0$. In the case of much stronger laser pulses of panels (b) and (c), we can find the plateau structure of $|J_x(\omega)|$, and it does not depend well on the existence of DC current. Here, “plateau” [86] means the frequency domain, in which the

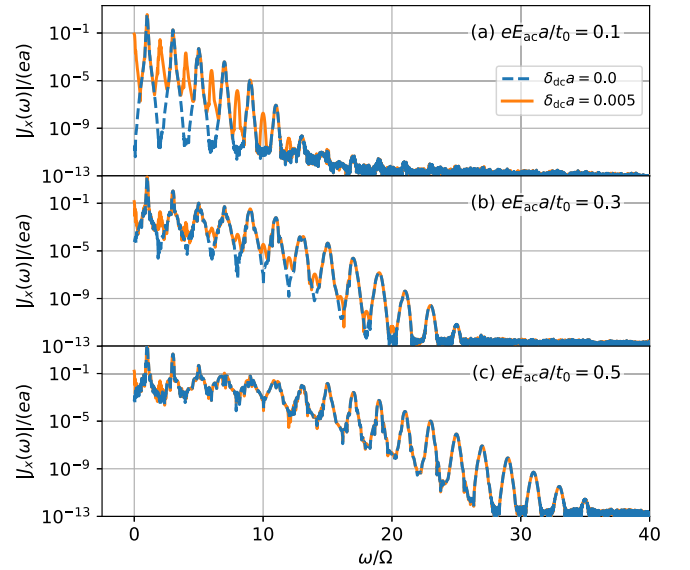


FIG. 10. HHG spectra $|J_x(\omega)|$ in laser-pulse driven graphene with/without a DC electric field E_{dc} at the chemical potential $\mu = 0.4t_0$ and the laser frequency $\Omega = \mu = 0.4t_0$. Panels (a), (b), and (c), respectively, correspond to $|J_x(\omega)|$ under the irradiation of laser strength $eE_{ac}a/t_0 = 0.1$, $eE_{ac}a/t_0 = 0.3$, and $eE_{ac}a/t_0 = 0.5$. Blue dotted and orange curves are, respectively, the results of $\delta_{dc}a = 0$ (zero DC current) and 0.005 (a finite DC current). The other parameters are chosen to be $\gamma = 0.1t_0$ and $\Delta = \epsilon = 0$.

HHG intensity is roughly independent of the frequency ω . In the present setup, the plateau seems to continue up to 10th-order harmonics (i.e., $\omega < 10\Omega$) for both cases (b) and (c).

On the other hand, we also find that for strong laser cases of (b) and (c), the even-order harmonics driven by DC current are quite small compared to odd-order harmonics or almost invisible. This is probably because the large linewidth of each odd-order harmonics covers the peak of neighboring even-order harmonics. Namely, this result indicates that we should apply a strong enough DC current to observe the DC-current-driven even-order harmonics in the case of the application of an extremely intense laser. However, as we mentioned in Sec. II B, we note that such a case with a large DC current is beyond the scope of the Boltzmann equation and the relaxation-time approximation.

IV. CONCLUSIONS

In this final section, we summarize and discuss the results of the present work. This paper theoretically investigates HHG spectra in the graphene model subjected to a DC electric field. Through the combination of the quantum master and Boltzmann equations, we numerically compute the HHG spectra with high accuracy and reveal their dependence on laser frequency, laser intensity, and DC current strength while accounting for the experimentally inevitable dissipation effects. The DC current induces an asymmetric shift of the Fermi surface, as shown in Fig. 2. Our numerical method provides a generic way of computing the HHG spectra of DC-current-driven electron systems from weak laser (perturbative) to strong laser (nonperturbative) regimes. The methodology is

explained in Sec. II. Compared with the previous studies for HHG in current-driven systems, our method makes it possible to observe higher-order (more than third-order) harmonic generations and HHG spectra in the nonperturbative regime.

Section III gives the numerical results of the present study. Throughout this section, we mainly consider the setup in which DC current is applied along the x axis, and the external laser is linearly polarized along the same x direction. In Sec. III A, we first show the shape of HHG spectra in a wide frequency regime in Fig. 3. The spectra, especially the presence or absence of n th-order harmonics, drastically change by tuning DC current, the laser ellipticity ϵ , and the staggered potential Δ . We find that this characteristic feature can be proved by the argument based on dynamical symmetry (see Table I). These results clearly indicate that HHG spectra can be moderately controlled with external tuning parameters such as DC current and the laser ellipticity.

In Sec. III B, we discuss the laser-frequency dependence of HHG spectra. The SHG peak displays a divergent behavior when the chemical potential and laser frequency approach zero, $\Omega = \mu \rightarrow 0$, in the weak-laser (perturbative) regime. However, in the strong-laser regime, the intensity tends to become stronger when $\Omega = \mu$ increases, as shown in Fig. 5. This behavior in the nonperturbative regime was first observed through our numerical method. We also argue that photoexcitations at the wave vectors around the DC-current-driven shifted Fermi surface are essential when we consider DC-current-driven harmonics (see Fig. 6).

Furthermore, when observing the fourth- and sixth-order harmonics for strong laser pulses (see Fig. 7), we find that the spectra cannot be explained by taking only interband optical transition processes, and the influence of intraband dynamics becomes more pronounced as the laser intensity increases.

In Sec. III D, we discuss the HHG spectra $I_y(\Omega)$ generated by the laser-driven current along the y axis, which appears only in the case of a finite staggered potential Δ . We find that as the laser intensity increases, multiple peak structures appear like other HHG spectra for a strong laser. In Sec. III E, we consider the case of extremely strong laser pulses. We observe a plateau regime in the HHG spectra, and we discuss the possibility that the DC current effect in HHG spectra becomes invisible as the laser intensity is extremely strong.

The present and recent works [48,49,72] indicate that the theoretical analysis based on the quantum master (GKSL) equation offers a powerful tool to compute optical nonlinear responses of many-body systems in a broad parameter regime.

Finally, we again comment on the limitations of our present approach. As discussed in Sec. II B, there are two important limitations. First, the chemical potential must be sufficiently far from the Dirac point energy, meaning a sufficiently large Fermi surface should exist. Secondly, our resultant HHG spectra are reliable only when they exhibit a linear behavior with respect to the DC electric field. These two conditions stem from the fact that the current-driven nonequilibrium steady state before the laser application is prepared by using the Boltzmann equation in our approach. However, we note that many experiments of HHG in current-driven electron systems

satisfy these conditions, and hence our approach is applicable to most such experiments.

ACKNOWLEDGMENTS

M.K. was supported by JST, the establishment of university fellowships towards the creation of science technology innovation, Grant No. JPMJFS2107, and by JST SPRING, Grant No. JPMJSP2109. M.S. was supported by JSPS KAKENHI (Grants No. 17K05513, No. 20H01830, and No. 20H01849) and a Grant-in-Aid for Scientific Research on Innovative Areas ‘‘Quantum Liquid Crystals’’ (Grant No. JP19H05825) and ‘‘Evolution of Chiral Materials Science using Helical Light Fields’’ (Grants No. JP22H05131 and No. JP23H04576).

APPENDIX A: SELECTION RULES FOR HHG

Here, we derive the selection rules for HHG from dynamical symmetries. These symmetries exactly hold in the case of a continuous-wave laser, i.e., $t_{\text{FWHM}} \rightarrow \infty$, whereas it is known that the selection rules derived from dynamical symmetries are often applicable even in laser-pulse cases of real experiments. In fact, our numerical results for laser pulses are consistent with such selection rules (see Fig. 3 and Table I). The selection rules below are all realized only in the case of the absence of the DC current, i.e., $\delta_{\text{dc}} = 0$.

1. LPL and x -direction inversion

First, we consider the irradiation of linearly polarized light (LPL) whose electric field is along the x direction. Since graphene has the symmetry of mirror operation for the x direction ($x \rightarrow -x$), the Hamiltonian $\hat{H}(t)$ satisfies the following dynamical symmetry:

$$\hat{U}_{\sigma_{yz}} \hat{H}(t + T/2) \hat{U}_{\sigma_{yz}}^\dagger = \hat{H}(t), \quad (\text{A1})$$

where $\hat{U}_{\sigma_{yz}}$ is the unitary operator of mirror operation for the x direction. Similarly, the current operator $\hat{\mathbf{J}}(t)$ satisfies

$$\hat{U}_{\sigma_{yz}} \hat{\mathbf{J}}(t + T/2) \hat{U}_{\sigma_{yz}}^\dagger = \begin{pmatrix} -\hat{J}_x(t) \\ \hat{J}_y(t) \end{pmatrix}. \quad (\text{A2})$$

As we will show soon later, these conditions are equivalent to

$$J_x(2n\Omega) = 0, \quad (\text{A3})$$

$$J_y[(2n+1)\Omega] = 0, \quad (\text{A4})$$

where n is an arbitrary integer. That is, in graphene illuminated by the LPL, the x -direction mirror symmetry results in the prohibition of even-order (odd-order) harmonics of J_x (J_y). Below, we prove Eqs. (A3) and (A4).

Through the Fourier transformation, the Hamiltonian and the current operator are represented as

$$\hat{H}(t) = \sum_k \hat{H}_k(t), \quad (\text{A5})$$

$$\hat{\mathbf{J}}(t) = \sum_k \hat{\mathbf{J}}_k(t). \quad (\text{A6})$$

These Fourier components with each wave vector \mathbf{k} satisfy

$$\hat{U}_{\sigma_{yz}} \hat{H}_{\mathbf{k}}(t + T/2) \hat{U}_{\sigma_{yz}}^\dagger = \hat{H}_{\mathbf{k}'}(t), \quad (\text{A7})$$

$$\hat{U}_{\sigma_{yz}} \hat{J}_{x,\mathbf{k}}(t + T/2) \hat{U}_{\sigma_{yz}}^\dagger = -\hat{J}_{x,\mathbf{k}'}(t), \quad (\text{A8})$$

$$\hat{U}_{\sigma_{yz}} \hat{J}_{y,\mathbf{k}}(t + T/2) \hat{U}_{\sigma_{yz}}^\dagger = \hat{J}_{y,\mathbf{k}'}(t), \quad (\text{A9})$$

where $\mathbf{k}' = (-k_x, k_y)$. Next, we consider the density matrix. Expressing the quantum master equation [Eq. (12)] symbolically using the Liouvillian superoperator $\mathcal{L}_{\mathbf{k}}(t)$, we have

$$\frac{d}{dt} \hat{\rho}_{\mathbf{k}}(t) = \mathcal{L}_{\mathbf{k}}(t) \hat{\rho}_{\mathbf{k}}(t). \quad (\text{A10})$$

Since the jump operators in our setup satisfy

$$\hat{U}_{\sigma_{yz}} \hat{L}_{\mathbf{k}} \hat{U}_{\sigma_{yz}}^\dagger = \hat{L}_{\mathbf{k}'}, \quad (\text{A11})$$

we obtain

$$\begin{aligned} \frac{d}{dt} \hat{\rho}_{\mathbf{k}'}(t) &= \mathcal{L}_{\mathbf{k}'}(t) \hat{\rho}_{\mathbf{k}'}(t) \\ &= \hat{U}_{\sigma_{yz}} \mathcal{L}_{\mathbf{k}}(t + T/2) \hat{U}_{\sigma_{yz}}^\dagger \hat{\rho}_{\mathbf{k}'}(t). \end{aligned} \quad (\text{A12})$$

Therefore, we arrive at

$$\frac{d}{dt} \hat{U}_{\sigma_{yz}}^\dagger \hat{\rho}_{\mathbf{k}'}(t) \hat{U}_{\sigma_{yz}} = \mathcal{L}_{\mathbf{k}}(t + T/2) \hat{U}_{\sigma_{yz}}^\dagger \hat{\rho}_{\mathbf{k}'}(t) \hat{U}_{\sigma_{yz}}. \quad (\text{A13})$$

By comparing Eq. (A13) with the original quantum master equation, we find the equality

$$\hat{U}_{\sigma_{yz}} \hat{\rho}_{\mathbf{k}}(t + T/2) \hat{U}_{\sigma_{yz}}^\dagger = \hat{\rho}_{\mathbf{k}'}(t). \quad (\text{A14})$$

This relation may be referred to as dynamical symmetry for the density matrix. From this dynamical symmetry, the Fourier component of the x -direction current satisfies the following relation:

$$\begin{aligned} J_{x,\mathbf{k}'}(t) &= \langle \hat{J}_{x,\mathbf{k}'}(t) \rangle_t \\ &= \text{Tr}[\hat{\rho}_{\mathbf{k}'}(t) \hat{J}_{x,\mathbf{k}'}(t)] \\ &= -\text{Tr}[\hat{\rho}_{\mathbf{k}}(t + T/2) \hat{J}_{x,\mathbf{k}}(t + T/2)] \\ &= -J_{x,\mathbf{k}}(t + T/2). \end{aligned} \quad (\text{A15})$$

Through a similar process for the y component of current, we obtain

$$J_{y,\mathbf{k}'}(t) = J_{y,\mathbf{k}}(t + T/2). \quad (\text{A16})$$

Here, from the pair of $J_{\alpha,\mathbf{k}}(t)$ and $J_{\alpha,\mathbf{k}'}(t)$, we define

$$\tilde{J}_{x,\mathbf{k}}(t) := J_{x,\mathbf{k}}(t) + J_{x,\mathbf{k}'}(t), \quad (\text{A17})$$

$$\tilde{J}_{y,\mathbf{k}}(t) := J_{y,\mathbf{k}}(t) + J_{y,\mathbf{k}'}(t). \quad (\text{A18})$$

We then find that they satisfy

$$\tilde{J}_{x,\mathbf{k}}(t) = -\tilde{J}_{x,\mathbf{k}}(t + T/2), \quad (\text{A19})$$

$$\tilde{J}_{y,\mathbf{k}}(t) = \tilde{J}_{y,\mathbf{k}}(t + T/2). \quad (\text{A20})$$

These results directly lead to the selection rules for the HHG spectrum as follows. The x component of the current,

$\tilde{J}_{x,\mathbf{k}}(n\Omega)$, is transformed as

$$\begin{aligned} \tilde{J}_{x,\mathbf{k}}(n\Omega) &= \int_0^T \frac{dt}{T} \tilde{J}_{x,\mathbf{k}}(t) e^{in\Omega t} \\ &= \int_{-T/2}^{T/2} \frac{dt}{T} \tilde{J}_{x,\mathbf{k}}(t + T/2) e^{in\Omega(t+T/2)} \\ &= -e^{in\Omega \frac{T}{2}} \int_{-T/2}^{T/2} \frac{dt}{T} \tilde{J}_{x,\mathbf{k}}(t) e^{in\Omega t} \\ &= -e^{in\pi} \tilde{J}_{x,\mathbf{k}}(n\Omega). \end{aligned} \quad (\text{A21})$$

Therefore, we have

$$\tilde{J}_{x,\mathbf{k}}(2m\Omega) = 0 \quad (m \in \mathbb{Z}). \quad (\text{A22})$$

Similarly, for $\tilde{J}_{y,\mathbf{k}}(n\Omega)$, we obtain

$$\tilde{J}_{y,\mathbf{k}}(n\Omega) = e^{in\pi} \tilde{J}_{y,\mathbf{k}}(n\Omega) \quad (\text{A23})$$

and

$$\tilde{J}_{y,\mathbf{k}}[(2m+1)\Omega] = 0 \quad (m \in \mathbb{Z}). \quad (\text{A24})$$

Taking the summation $\sum_{k_x > 0} \tilde{J}_{\alpha,\mathbf{k}}(n\Omega)$ in the positive- k_x region of the Brillouin zone, we finally arrive at Eqs. (A3) and (A4).

2. CPL and n -fold rotation in the x - y plane

Next, we consider the case of the application of circularly polarized light (CPL) to a two-dimensional (2D) electron system on the x - y plane. Here, the electric field of CPL is in the same x - y plane. We assume that a CPL-driven 2D system in the x - y plane satisfies the following symmetry relations:

$$\hat{H}_{\mathbf{k}}(t) = \hat{U}_n \hat{H}_{\mathcal{R}_n \mathbf{k}}(t + T/n) \hat{U}_n^\dagger, \quad (\text{A25})$$

$$\hat{J}_{\mathbf{k}}(t) = \hat{U}_n \mathcal{R}_n \hat{J}_{\mathcal{R}_n \mathbf{k}}(t + T/n) \hat{U}_n^\dagger, \quad (\text{A26})$$

where \hat{U}_n is the unitary operator of $2\pi/n$ -degree rotation in the x - y plane, and \mathcal{R}_n is the 2×2 matrix for an in-plane rotation by $2\pi/n$, which acts on vector quantities. In graphene models, as mentioned in Table I of the main text, the above relations hold for $n = 2$ and 3. We note that when 2D electron systems are irradiated by the CPL, its electric field rotates by $2\pi/n$ during the time interval T/n .

For the above discrete-rotation symmetric system, we then consider the time evolution of the density matrix. Similarly to Appendix A1, the quantum master equation [Eq. (12)] is expressed as

$$\frac{d}{dt} \hat{\rho}_{\mathbf{k}}(t) = \mathcal{L}_{\mathbf{k}}(t) \hat{\rho}_{\mathbf{k}}(t). \quad (\text{A27})$$

Assuming the jump operators satisfy

$$\hat{L}_{\mathbf{k}} = \hat{U}_n \hat{L}_{\mathcal{R}_n \mathbf{k}} \hat{U}_n^\dagger, \quad (\text{A28})$$

we obtain

$$\begin{aligned} \frac{d}{dt} \hat{\rho}_{\mathbf{k}}(t) &= \mathcal{L}_{\mathbf{k}}(t) \hat{\rho}_{\mathbf{k}}(t) \\ &= \hat{U}_n \mathcal{L}_{\mathcal{R}_n \mathbf{k}}(t + T/n) \hat{U}_n^\dagger \hat{\rho}_{\mathbf{k}}(t). \end{aligned} \quad (\text{A29})$$

Therefore, we find

$$\frac{d}{dt} \hat{U}_n^\dagger \hat{\rho}_{\mathbf{k}}(t) \hat{U}_n = \mathcal{L}_{\mathcal{R}_n \mathbf{k}}(t + T/n) \hat{U}_n^\dagger \hat{\rho}_{\mathbf{k}}(t) \hat{U}_n. \quad (\text{A30})$$

Comparing this result with the original quantum master equation, we obtain

$$\hat{\rho}_k(t) = \hat{U}_n \hat{\rho}_{\mathcal{R}_n k}(t + T/n) \hat{U}_n^\dagger. \quad (\text{A31})$$

Through this dynamical symmetry of the density matrix, the k component of the current is computed as follows:

$$\begin{aligned} \mathbf{J}_k(t) &= \langle \hat{\mathbf{J}}_k(t) \rangle_t = \text{Tr}[\hat{\rho}_k(t) \hat{\mathbf{J}}_k(t)] \\ &= \mathcal{R}_n \text{Tr}[\hat{\rho}_{\mathcal{R}_n k}(t + T/n) \hat{\mathbf{J}}_{\mathcal{R}_n k}(t + T/n)] \\ &= \mathcal{R}_n \mathbf{J}_{\mathcal{R}_n k}(t + T/n). \end{aligned} \quad (\text{A32})$$

Considering this relation about the rotating operations, we introduce a new quantity

$$\tilde{\mathbf{J}}_k(t) := \sum_{\ell=0}^{n-1} \mathbf{J}_{(\mathcal{R}_n)^\ell k}(t). \quad (\text{A33})$$

Then, we find that it satisfies

$$\begin{aligned} \tilde{\mathbf{J}}_k(t) &= \mathcal{R}_n \tilde{\mathbf{J}}_k(t + T/n) = (\mathcal{R}_n)^2 \tilde{\mathbf{J}}_k(t + 2T/n) \\ &= \dots = (\mathcal{R}_n)^{n-1} \tilde{\mathbf{J}}_k[t + (n-1)T/n]. \end{aligned} \quad (\text{A34})$$

Equation (A34) enables us to derive the selection rules for the HHG spectrum. From the equation, the Fourier component of the current in time direction, $\mathbf{J}(m\Omega)$, is given by

$$\begin{aligned} \tilde{\mathbf{J}}_k(m\Omega) &= \mathcal{R}_n e^{i2m\pi/n} \tilde{\mathbf{J}}_k(m\Omega) = (\mathcal{R}_n)^2 e^{i4m\pi/n} \tilde{\mathbf{J}}_k(m\Omega) \\ &= \dots = (\mathcal{R}_n)^{n-1} e^{i2(n-1)m\pi/n} \tilde{\mathbf{J}}_k(m\Omega). \end{aligned} \quad (\text{A35})$$

If we consider the case of $m = n\ell$ ($\ell \in \mathbb{Z}$), we obtain

$$\begin{aligned} \tilde{\mathbf{J}}_k(n\ell\Omega) &= \frac{1}{n} (1 + \mathcal{R}_n + (\mathcal{R}_n)^2 + \dots + (\mathcal{R}_n)^{n-1}) \tilde{\mathbf{J}}_k(n\ell\Omega). \end{aligned} \quad (\text{A36})$$

Thus we have $\tilde{\mathbf{J}}_k(n\ell\Omega) = \mathbf{0}$. Taking the proper summation of $\tilde{\mathbf{J}}_k(n\ell\Omega)$ over the Brillouin zone, we finally obtain

$$\mathbf{J}(n\ell\Omega) = \mathbf{0}. \quad (\text{A37})$$

This means that the $n\ell$ th order harmonics with $n = 2$ and 3 disappear in graphene models under the irradiation of circularly polarized light.

3. Breakdown of dynamical symmetry by applying DC current

The dynamical symmetry of the density matrix is broken by applying a DC current, and it usually accompanies the appearance of the harmonics forbidden by the dynamical symmetry. In the case of Appendix A 1, the breakdown of the dynamical symmetry means the following inequality:

$$\hat{\rho}_k(t) \neq \hat{U}_{\sigma_{yz}} \hat{\rho}_{k'}(t + T/2) \hat{U}_{\sigma_{yz}}^\dagger. \quad (\text{A38})$$

In this section, we discuss why this inequality is generally realized in the case of applying a DC current.

When we have a finite DC current, the initial state before the application of a laser is given by $\hat{\rho}_k = |g_{k+\delta_{dc}}\rangle\langle g_{k+\delta_{dc}}|$. This density matrix of the NESS clearly breaks the mirror symmetry of $\hat{U}_{\sigma_{yz}}$, as shown in Fig. 2(a). This could be a simple answer to why the inequality of Eq. (A38) holds.

We also try to construct a more serious argument for Eq. (A38). We first assume that the density matrix at the initial

time $t = t_0$ is given by $\hat{\rho}_k = |g_{k+\delta_{dc}}\rangle\langle g_{k+\delta_{dc}}| (|g_k\rangle\langle g_k|)$ for the case of a finite (zero) DC current. Then, a continuous-wave laser ($t_{\text{FWHM}} \rightarrow \infty$) is assumed to be adiabatically introduced. Under this setup, let us first consider the case without DC current. As discussed in Appendix A 1, when $\delta_{dc} = 0$,

$$\mathcal{L}_k(t) = \hat{U}_{\sigma_{yz}} \mathcal{L}_{k'}(t + T/2) \hat{U}_{\sigma_{yz}}^\dagger \quad (\text{A39})$$

holds. Therefore, we can expect that the time-evolution super-operator $\mathcal{V}_k(t, t_0) = \mathcal{T} \exp(\int_{t_0}^t \mathcal{L}_k(s) ds)$ satisfies

$$\mathcal{V}_k(t, t_0) = \hat{U}_{\sigma_{yz}} \mathcal{V}_{k'}(t + T/2, t_0) \hat{U}_{\sigma_{yz}}^\dagger \quad (\text{A40})$$

if t is sufficiently far from t_0 . Here, \mathcal{T} represents the time-ordered product. This relation directly leads to Eq. (A14) as follows:

$$\begin{aligned} &\hat{U}_{\sigma_{yz}} \hat{\rho}_{k'}(t + T/2) \hat{U}_{\sigma_{yz}}^\dagger \\ &= \hat{U}_{\sigma_{yz}} \mathcal{V}_{k'}(t + T/2, t_0) \hat{U}_{\sigma_{yz}}^\dagger \hat{U}_{\sigma_{yz}} \hat{\rho}_{k'} \hat{U}_{\sigma_{yz}}^\dagger \\ &= \mathcal{V}_k(t, t_0) \hat{\rho}_k \\ &= \hat{\rho}_k(t). \end{aligned} \quad (\text{A41})$$

Here, $\hat{\rho}_k := \hat{\rho}_k(t_0) = |g_k\rangle\langle g_k|$, and we have used $\hat{U}_{\sigma_{yz}} \hat{\rho}_{k'} \hat{U}_{\sigma_{yz}}^\dagger = \hat{U}_{\sigma_{yz}} |g_{k'}\rangle\langle g_{k'}| \hat{U}_{\sigma_{yz}}^\dagger = |g_k\rangle\langle g_k| = \hat{\rho}_k$.

Next, we consider the case of $\delta_{dc} \neq 0$, in which the density matrix at $t = t_0$ is given by $\hat{\rho}_k = |g_{k+\delta_{dc}}\rangle\langle g_{k+\delta_{dc}}|$. As we mentioned, this density matrix follows

$$\begin{aligned} \hat{U}_{\sigma_{yz}} \hat{\rho}_{k'} \hat{U}_{\sigma_{yz}}^\dagger &= \hat{U}_{\sigma_{yz}} |g_{k'+\delta_{dc}}\rangle\langle g_{k'+\delta_{dc}}| \hat{U}_{\sigma_{yz}}^\dagger \\ &= |g_{k+\delta'_{dc}}\rangle\langle g_{k+\delta'_{dc}}| \\ &\neq \hat{\rho}_k, \end{aligned} \quad (\text{A42})$$

where we have introduced the new symbol $\delta'_{dc} = (-\delta_{dc}^x, \delta_{dc}^y)$. In addition, for $\delta_{dc} \neq 0$, we have

$$\hat{U}_{\sigma_{yz}} \hat{L}_k \hat{U}_{\sigma_{yz}}^\dagger \neq \hat{L}_{k'}. \quad (\text{A43})$$

This leads to

$$\mathcal{V}_k(t, t_0) \neq \hat{U}_{\sigma_{yz}} \mathcal{V}_{k'}(t + T/2, t_0) \hat{U}_{\sigma_{yz}}^\dagger. \quad (\text{A44})$$

From these two inequalities of Eqs. (A42) and (A44), we can say that Eq. (A38) generally holds when we apply a DC current. In discrete-rotation symmetric systems in Appendix A 2, we can also make an argument in a similar way that the dynamical symmetry is generally broken by a DC current.

APPENDIX B: RELATIONSHIP BETWEEN THE MASTER EQUATION AND THE BLOCH EQUATION

This Appendix briefly shows the relationship between the quantum master equation and the optical Bloch equation [87].

We start from the master equation we have adopted:

$$\begin{aligned} \frac{d\hat{\rho}_k(t)}{dt} &= -i[\hat{H}_k(t), \hat{\rho}_k(t)] \\ &+ \gamma \left(\hat{L}_k \hat{\rho}_k(t) \hat{L}_k^\dagger - \frac{1}{2} \{ \hat{L}_k^\dagger \hat{L}_k, \hat{\rho}_k(t) \} \right). \end{aligned} \quad (\text{B1})$$

This is the equation for a k -diagonal two-band system, including a simple relaxation process by the jump operator

$\hat{L}_k = |g_k\rangle\langle e_k|$. In two-level systems, any Hermitian operator \hat{A} can be expressed using identity operator \hat{I} and Pauli operators $\hat{\sigma} = (\hat{\sigma}^x, \hat{\sigma}^y, \hat{\sigma}^z)$ as

$$\hat{A} = A_0\hat{I} + \mathbf{A} \cdot \hat{\sigma}, \quad (\text{B2})$$

where $\mathbf{A} = (A_x, A_y, A_z)$ is a three-dimensional vector and $A_{0,x,y,z} \in \mathbb{R}$. Hence, the product of two Hermitian operators is given by

$$\hat{A}\hat{B} = (A_0B_0 + \mathbf{A} \cdot \mathbf{B})\hat{I} + (A_0\mathbf{B} + B_0\mathbf{A} + i\mathbf{A} \times \mathbf{B}) \cdot \hat{\sigma}. \quad (\text{B3})$$

Since the Hamiltonian $\hat{H}_k(t)$ and the density matrix $\hat{\rho}_k(t)$ are both Hermitian, they may be expressed as $\hat{H}_k(t) = \mathbf{h}_k(t) \cdot \hat{\sigma}$ and $\hat{\rho}_k(t) = \tau_k^0(t)\hat{I} + \boldsymbol{\tau}_k(t) \cdot \hat{\sigma}$. Here, we have introduced real vector quantities $\mathbf{h}_k(t)$ and $\boldsymbol{\tau}_k(t)$ and a real scalar quantity $\tau_k^0(t)$. The jump operator is not generally a Hermitian operator, but in the present model it can also be written by using Pauli matrices as follows:

$$\hat{L}_k = \mathbf{L}_k \cdot \hat{\sigma}, \quad (\text{B4})$$

with the complex coefficients $\mathbf{L}_k = (L_k^x, L_k^y, L_k^z)$. Since the jump operator we used is $\hat{L}_k = |g_k\rangle\langle e_k| = (\hat{\sigma}^x - i\hat{\sigma}^y)/2$, the coefficient is given by $\mathbf{L}_k = (1/2, -i/2, 0)$.

Substituting the 2×2 forms of the Hamiltonian, the density matrix, and the jump operator into Eq. (B1) and then using Eq. (B3), we obtain

$$\begin{aligned} \frac{d\tau_k^0}{dt}\hat{I} + \left(\frac{d\boldsymbol{\tau}_k}{dt} - 2\mathbf{h}_k \times \boldsymbol{\tau}_k - 2\gamma[\text{Re}[(\mathbf{L}_k \cdot \boldsymbol{\tau}_k)\mathbf{L}_k^*] \right. \\ \left. - |\mathbf{L}_k|^2\boldsymbol{\tau}_k + i\tau_k^0\mathbf{L}_k \times \mathbf{L}_k^* \right) \cdot \hat{\sigma} = 0. \end{aligned} \quad (\text{B5})$$

This can be viewed as coupled differential equations for τ_k^0 and $\boldsymbol{\tau}_k$. Focusing on the coefficient of \hat{I} , we have $\frac{d\tau_k^0}{dt} = 0$, and its solution is given by $\tau_k^0(t) = 1$ because of the normalization of the density matrix. The remaining vector $\boldsymbol{\tau}_k(t)$ satisfies

$$\begin{aligned} \frac{d\boldsymbol{\tau}_k}{dt} = 2\mathbf{h}_k \times \boldsymbol{\tau}_k \\ + 2\gamma[\text{Re}[(\mathbf{L}_k \cdot \boldsymbol{\tau}_k)\mathbf{L}_k^*] - |\mathbf{L}_k|^2\boldsymbol{\tau}_k + i\mathbf{L}_k \times \mathbf{L}_k^*]. \end{aligned} \quad (\text{B6})$$

Substituting $\mathbf{L}_k = (1/2, -i/2, 0)$, we arrive at

$$\frac{d}{dt}\boldsymbol{\tau}_k(t) = 2\mathbf{h}_k(t) \times \boldsymbol{\tau}_k(t) - \begin{pmatrix} \frac{\gamma}{2}\tau_{x,k}(t) \\ \frac{\gamma}{2}\tau_{y,k}(t) \\ \gamma(\tau_{z,k}(t) - \langle\tau_{z,k}\rangle) \end{pmatrix}, \quad (\text{B7})$$

where $\langle\tau_{z,k}\rangle = -1$. This is nothing but a Bloch equation whose longitudinal and transverse relaxation times, T_1 and T_2 , are given by

$$T_1 = \frac{1}{\gamma}, \quad T_2 = \frac{2}{\gamma}. \quad (\text{B8})$$

Namely, our simple setup of the jump operator includes both longitudinal and transverse relaxation processes, satisfying the detailed balance condition at $T = 0$.

In the present study, we have adopted a simple but realistic relaxation (jump) operator, while in general, the GKSL equation can describe wider sorts of dissipation processes rather than the Bloch equation [71,87,88]. Namely, in the mathematical sense, the Bloch equation is included within the framework of the GKSL equation.

We note that theoretical studies beyond the above relaxation-time approximation have also progressed [89–91]. For instance, the quantum kinetic equation approach based on the Green's functions [87,92] can describe the effects of various scattering processes, in principle, from the microscopic viewpoint. However, it is generally difficult to simultaneously treat light-matter couplings, interactions, and impurity scatterings within the analytic quantum kinetic approach. In fact, most of the previous quantum kinetic approaches for HHG take these effects into account in a perturbative manner, where only lower-order harmonics can be computed [93,94]. On the other hand, our numerical approach using the GKSL equation with a phenomenological relaxation time can analyze weak-to-strong light-induced nonequilibrium phenomena, especially the intense-laser-driven nonperturbative effects. As discussed in Sec. III B, the analytic, perturbative approach and our numerical one are complementary with each other.

-
- [1] S. Ghimire and D. A. Reis, High-harmonic generation from solids, *Nat. Phys.* **15**, 10 (2019).
- [2] L. Yue and M. B. Gaarde, Introduction to theory of high-harmonic generation in solids: Tutorial, *J. Opt. Soc. Am. B* **39**, 535 (2022).
- [3] L. Li, P. Lan, X. Zhu, and P. Lu, High harmonic generation in solids: Particle and wave perspectives, *Rep. Prog. Phys.* **86**, 116401 (2023).
- [4] U. Bhattacharya, T. Lamprou, A. S. Maxwell, A. Ordóñez, E. Pisanty, J. Rivera-Dean, P. Stammer, M. F. Ciappina, M. Lewenstein, and P. Tzallas, Strong–laser–field physics, nonclassical light states and quantum information science, *Rep. Prog. Phys.* **86**, 094401 (2023).
- [5] H. Hirori, S. A. Sato, and Y. Kanemitsu, High-order harmonic generation in solids: The role of intraband transitions in extreme nonlinear optics, *J. Phys. Chem. Lett.* **15**, 2184 (2024).
- [6] S. M. Young and A. M. Rappe, First principles calculation of the shift current photovoltaic effect in ferroelectrics, *Phys. Rev. Lett.* **109**, 116601 (2012).
- [7] L. Z. Tan, F. Zheng, S. M. Young, F. Wang, S. Liu, and A. M. Rappe, Shift current bulk photovoltaic effect in polar materials—hybrid and oxide perovskites and beyond, *npj Comput. Mater.* **2**, 16026 (2016).
- [8] T. Morimoto and N. Nagaosa, Topological nature of nonlinear optical effects in solids, *Sci. Adv.* **2**, e1501524 (2016).
- [9] Y. Tokura and N. Nagaosa, Nonreciprocal responses from noncentrosymmetric quantum materials, *Nat. Commun.* **9**, 3740 (2018).
- [10] H. Ishizuka and M. Sato, Rectification of spin current in inversion-asymmetric magnets with linearly polarized electromagnetic waves, *Phys. Rev. Lett.* **122**, 197702 (2019).

- [11] B. I. Sturman and V. M. Fridkin, *The Photovoltaic and Photo-refractive Effects in Noncentrosymmetric Materials*, 1st ed. (Routledge, London, 1992).
- [12] H. Watanabe and Y. Yanase, Chiral photocurrent in parity-violating magnet and enhanced response in topological antiferromagnet, *Phys. Rev. X* **11**, 011001 (2021).
- [13] H. Ishizuka and M. Sato, Peltier effect of phonon driven by ac electromagnetic waves, [arXiv:2310.03271](https://arxiv.org/abs/2310.03271) [cond-mat].
- [14] A. Eckardt and E. Anisimovas, High-frequency approximation for periodically driven quantum systems from a Floquet-space perspective, *New J. Phys.* **17**, 093039 (2015).
- [15] T. Mikami, S. Kitamura, K. Yasuda, N. Tsuji, T. Oka, and H. Aoki, Brillouin-Wigner theory for high-frequency expansion in periodically driven systems: Application to Floquet topological insulators, *Phys. Rev. B* **93**, 144307 (2016).
- [16] T. Mori, T. Kuwahara, and K. Saito, Rigorous bound on energy absorption and generic relaxation in periodically driven quantum systems, *Phys. Rev. Lett.* **116**, 120401 (2016).
- [17] T. Kuwahara, T. Mori, and K. Saito, Floquet–Magnus theory and generic transient dynamics in periodically driven many-body quantum systems, *Ann. Phys.* **367**, 96 (2016).
- [18] A. Eckardt, Colloquium: Atomic quantum gases in periodically driven optical lattices, *Rev. Mod. Phys.* **89**, 011004 (2017).
- [19] T. Oka and S. Kitamura, Floquet engineering of quantum materials, *Annu. Rev. Condens. Matter Phys.* **10**, 387 (2019).
- [20] M. Sato, Floquet theory and ultrafast control of magnetism, in *Chirality, Magnetism and Magnetoelectricity*, edited by E. Kamenetskii (Springer International, Cham, 2021), Vol. 138, pp. 265–286.
- [21] A. McPherson, G. Gibson, H. Jara, U. Johann, T. S. Luk, I. A. McIntyre, K. Boyer, and C. K. Rhodes, Studies of multiphoton production of vacuum-ultraviolet radiation in the rare gases, *J. Opt. Soc. Am. B* **4**, 595 (1987).
- [22] M. Ferray, A. L’Huillier, X. F. Li, L. A. Lompre, G. Mainfray, and C. Manus, Multiple-harmonic conversion of 1064 nm radiation in rare gases, *J. Phys. B* **21**, L31 (1988).
- [23] J. L. Krause, K. J. Schafer, and K. C. Kulander, High-order harmonic generation from atoms and ions in the high intensity regime, *Phys. Rev. Lett.* **68**, 3535 (1992).
- [24] P. B. Corkum, Plasma perspective on strong field multiphoton ionization, *Phys. Rev. Lett.* **71**, 1994 (1993).
- [25] K. J. Schafer, B. Yang, L. F. DiMauro, and K. C. Kulander, Above threshold ionization beyond the high harmonic cutoff, *Phys. Rev. Lett.* **70**, 1599 (1993).
- [26] J. J. Macklin, J. D. Kmetec, and C. L. Gordon, High-order harmonic generation using intense femtosecond pulses, *Phys. Rev. Lett.* **70**, 766 (1993).
- [27] S. Ghimire, A. D. DiChiara, E. Sistrunk, P. Agostini, L. F. DiMauro, and D. A. Reis, Observation of high-order harmonic generation in a bulk crystal, *Nat. Phys.* **7**, 138 (2011).
- [28] O. Schubert, M. Hohenleutner, F. Langer, B. Urbanek, C. Lange, U. Huttner, D. Golde, T. Meier, M. Kira, S. W. Koch, and R. Huber, Sub-cycle control of terahertz high-harmonic generation by dynamical Bloch oscillations, *Nat. Photon.* **8**, 119 (2014).
- [29] G. Vampa, C. R. McDonald, G. Orlando, P. B. Corkum, and T. Brabec, Semiclassical analysis of high harmonic generation in bulk crystals, *Phys. Rev. B* **91**, 064302 (2015).
- [30] T. T. Luu, M. Garg, S. Y. Kruchinin, A. Moulet, M. T. Hassan, and E. Goulielmakis, Extreme ultraviolet high-harmonic spectroscopy of solids, *Nature (London)* **521**, 498 (2015).
- [31] B. Liu, H. Bromberger, A. Cartella, T. Gebert, M. Först, and A. Cavalleri, Generation of narrowband, high-intensity, carrier-envelope phase-stable pulses tunable between 4 and 18 THz, *Opt. Lett.* **42**, 129 (2017).
- [32] Y. S. You, D. A. Reis, and S. Ghimire, Anisotropic high-harmonic generation in bulk crystals, *Nat. Phys.* **13**, 345 (2017).
- [33] G. Vampa, T. J. Hammond, M. Taucer, X. Ding, X. Ropagnol, T. Ozaki, S. Delprat, M. Chaker, N. Thiré, B. E. Schmidt, F. Légaré, D. D. Klug, A. Y. Naumov, D. M. Villeneuve, A. Staudte, and P. B. Corkum, Strong-field optoelectronics in solids, *Nat. Photon.* **12**, 465 (2018).
- [34] P. Xia, C. Kim, F. Lu, T. Kanai, H. Akiyama, J. Itatani, and N. Ishii, Nonlinear propagation effects in high harmonic generation in reflection and transmission from gallium arsenide, *Opt. Express* **26**, 29393 (2018).
- [35] N. Yoshikawa, K. Nagai, K. Uchida, Y. Takaguchi, S. Sasaki, Y. Miyata, and K. Tanaka, Interband resonant high-harmonic generation by valley polarized electron–Hole pairs, *Nat. Commun.* **10**, 3709 (2019).
- [36] H. Lakhotia, H. Y. Kim, M. Zhan, S. Hu, S. Meng, and E. Goulielmakis, Laser picoscopy of valence electrons in solids, *Nature (London)* **583**, 55 (2020).
- [37] R. Matsunaga, N. Tsuji, H. Fujita, A. Sugioka, K. Makise, Y. Uzawa, H. Terai, Z. Wang, H. Aoki, and R. Shimano, Light-induced collective pseudospin precession resonating with Higgs mode in a superconductor, *Science* **345**, 1145 (2014).
- [38] N. Yoshikawa, T. Tamaya, and K. Tanaka, High-harmonic generation in graphene enhanced by elliptically polarized light excitation, *Science* **356**, 736 (2017).
- [39] H. A. Hafez, S. Kovalev, J.-C. Deinert, Z. Mics, B. Green, N. Awari, M. Chen, S. Germanskiy, U. Lehnert, J. Teichert, Z. Wang, K.-J. Tielrooij, Z. Liu, Z. Chen, A. Narita, K. Müllen, M. Bonn, M. Gensch, and D. Turchinovich, Extremely efficient terahertz high-harmonic generation in graphene by hot Dirac fermions, *Nature (London)* **561**, 507 (2018).
- [40] S. Kovalev, R. M. A. Dantas, S. Germanskiy, J.-C. Deinert, B. Green, I. Ilyakov, N. Awari, M. Chen, M. Bawatna, J. Ling, F. Xiu, P. H. M. Van Loosdrecht, P. Surówka, T. Oka, and Z. Wang, Non-perturbative terahertz high-harmonic generation in the three-dimensional Dirac semimetal Cd₃As₂, *Nat. Commun.* **11**, 2451 (2020).
- [41] B. Cheng, N. Kanda, T. N. Ikeda, T. Matsuda, P. Xia, T. Schumann, S. Stemmer, J. Itatani, N. P. Armitage, and R. Matsunaga, Efficient terahertz harmonic generation with coherent acceleration of electrons in the Dirac semimetal Cd₃As₂, *Phys. Rev. Lett.* **124**, 117402 (2020).
- [42] Y. Murakami, M. Eckstein, and P. Werner, High-harmonic generation in mott insulators, *Phys. Rev. Lett.* **121**, 057405 (2018).
- [43] M. R. Bionta, E. Haddad, A. Leblanc, V. Gruson, P. Lassonde, H. Ibrahim, J. Chaillou, N. Émond, M. R. Otto, Á. Jiménez-Galán, R. E. F. Silva, M. Ivanov, B. J. Siwick, M. Chaker, and F. Légaré, Tracking ultrafast solid-state dynamics using high harmonic spectroscopy, *Phys. Rev. Res.* **3**, 023250 (2021).
- [44] O. Grånäs, I. Vaskivskiy, X. Wang, P. Thunström, S. Ghimire, R. Knut, J. Söderström, L. Kjellsson, D. Turenne, R. Y. Engel, M. Beye, J. Lu, D. J. Higley, A. H. Reid, W. Schlotter, G. Coslovich, M. Hoffmann, G. Kolesov, C. Schüßler-Langeheine,

- A. Styervoyedov *et al.*, Ultrafast modification of the electronic structure of a correlated insulator, *Phys. Rev. Res.* **4**, L032030 (2022).
- [45] K. Uchida, G. Mattoni, S. Yonezawa, F. Nakamura, Y. Maeno, and K. Tanaka, High-order Harmonic generation and its unconventional scaling law in the Mott-insulating Ca_2RuO_4 , *Phys. Rev. Lett.* **128**, 127401 (2022).
- [46] S. Baierl, J. H. Mentink, M. Hohenleutner, L. Braun, T.-M. Do, C. Lange, A. Sell, M. Fiebig, G. Woltersdorf, T. Kampfrath, and R. Huber, Terahertz-driven nonlinear spin response of antiferromagnetic nickel oxide, *Phys. Rev. Lett.* **117**, 197201 (2016).
- [47] J. Lu, X. Li, H. Y. Hwang, B. K. Ofori-Okai, T. Kurihara, T. Suemoto, and K. A. Nelson, Coherent two-dimensional terahertz magnetic resonance spectroscopy of collective spin waves, *Phys. Rev. Lett.* **118**, 207204 (2017).
- [48] T. N. Ikeda and M. Sato, High-harmonic generation by electric polarization, spin current, and magnetization, *Phys. Rev. B* **100**, 214424 (2019).
- [49] M. Kanega, T. N. Ikeda, and M. Sato, Linear and nonlinear optical responses in Kitaev spin liquids, *Phys. Rev. Res.* **3**, L032024 (2021).
- [50] Z. Zhang, F. Sekiguchi, T. Moriyama, S. C. Furuya, M. Sato, T. Satoh, Y. Mukai, K. Tanaka, T. Yamamoto, H. Kageyama, Y. Kanemitsu, and H. Hirori, Generation of third-Harmonic spin oscillation from strong spin precession induced by terahertz magnetic near fields, *Nat. Commun.* **14**, 1795 (2023).
- [51] S. Takayoshi, Y. Murakami, and P. Werner, High-harmonic generation in quantum spin systems, *Phys. Rev. B* **99**, 184303 (2019).
- [52] O. Neufeld, D. Podolsky, and O. Cohen, Floquet group theory and its application to selection rules in harmonic generation, *Nat. Commun.* **10**, 405 (2019).
- [53] S. Sze and K. K. Ng, *Physics of Semiconductor Devices*, 3rd ed. (Wiley, New York, 2006).
- [54] H. Li, F. Li, Z. Shen, S.-T. Han, J. Chen, C. Dong, C. Chen, Y. Zhou, and M. Wang, Photoferroelectric perovskite solar cells: Principles, advances and insights, *Nano Today* **37**, 101062 (2021).
- [55] L. Wu, S. Patankar, T. Morimoto, N. L. Nair, E. Thewalt, A. Little, J. G. Analytis, J. E. Moore, and J. Orenstein, Giant anisotropic nonlinear optical response in transition metal monpnictide Weyl semimetals, *Nat. Phys.* **13**, 350 (2017).
- [56] S. Patankar, L. Wu, B. Lu, M. Rai, J. D. Tran, T. Morimoto, D. E. Parker, A. G. Grushin, N. L. Nair, J. G. Analytis, J. E. Moore, J. Orenstein, and D. H. Torchinsky, Resonance-enhanced optical nonlinearity in the Weyl semimetal TaAs, *Phys. Rev. B* **98**, 165113 (2018).
- [57] G. B. Osterhoudt, L. K. Diebel, M. J. Gray, X. Yang, J. Stanco, X. Huang, B. Shen, N. Ni, P. J. W. Moll, Y. Ran, and K. S. Burch, Colossal mid-infrared bulk photovoltaic effect in a type-I Weyl semimetal, *Nat. Mater.* **18**, 471 (2019).
- [58] N. Sirica, R. I. Tobey, L. X. Zhao, G. F. Chen, B. Xu, R. Yang, B. Shen, D. A. Yarotski, P. Bowlan, S. A. Trugman, J.-X. Zhu, Y. M. Dai, A. K. Azad, N. Ni, X. G. Qiu, A. J. Taylor, and R. P. Prasankumar, Tracking ultrafast photocurrents in the Weyl semimetal TaAs using THz emission spectroscopy, *Phys. Rev. Lett.* **122**, 197401 (2019).
- [59] J. B. Khurgin, Current induced second harmonic generation in semiconductors, *Appl. Phys. Lett.* **67**, 1113 (1995).
- [60] S. Wu, L. Mao, A. M. Jones, W. Yao, C. Zhang, and X. Xu, Quantum-enhanced tunable second-order optical nonlinearity in bilayer graphene, *Nano Lett.* **12**, 2032 (2012).
- [61] J. L. Cheng, N. Vermeulen, and J. E. Sipe, DC current induced second order optical nonlinearity in graphene, *Opt. Express* **22**, 15868 (2014).
- [62] K. Takasan, T. Morimoto, J. Orenstein, and J. E. Moore, Current-induced second harmonic generation in inversion-symmetric Dirac and Weyl semimetals, *Phys. Rev. B* **104**, L161202 (2021).
- [63] Y. Gao and F. Zhang, Current-induced second harmonic generation of Dirac or Weyl semimetals in a strong magnetic field, *Phys. Rev. B* **103**, L041301 (2021).
- [64] O. A. Aktsipetrov, V. O. Bessonov, A. A. Fedyanin, and V. O. Val'dner, DC-induced generation of the reflected second harmonic in silicon, *JETP Lett.* **89**, 58 (2009).
- [65] B. A. Ruzicka, L. K. Werake, G. Xu, J. B. Khurgin, E. Ya. Sherman, J. Z. Wu, and H. Zhao, Second-harmonic generation induced by electric currents in GaAs, *Phys. Rev. Lett.* **108**, 077403 (2012).
- [66] A. Y. Bykov, T. V. Murzina, M. G. Rybin, and E. D. Obraztsova, Second harmonic generation in multilayer graphene induced by direct electric current, *Phys. Rev. B* **85**, 121413(R) (2012).
- [67] Y. Q. An, F. Nelson, J. U. Lee, and A. C. Diebold, Enhanced optical second-harmonic generation from the current-biased graphene/SiO₂/Si(001) structure, *Nano Lett.* **13**, 2104 (2013).
- [68] S. Nakamura, K. Katsumi, H. Terai, and R. Shimano, Nonreciprocal terahertz second-harmonic generation in superconducting NbN under supercurrent injection, *Phys. Rev. Lett.* **125**, 097004 (2020).
- [69] V. Gorini, A. Kossakowski, and E. C. G. Sudarshan, Completely positive dynamical semigroups of N -level systems, *J. Math. Phys.* **17**, 821 (1976).
- [70] G. Lindblad, On the generators of quantum dynamical semigroups, *Commun. Math. Phys.* **48**, 119 (1976).
- [71] H.-P. Breuer and F. Petruccione, *The Theory of Open Quantum Systems*, 1st ed. (Oxford University Press, Oxford, 2007).
- [72] M. Sato and Y. Morisaku, Two-photon driven magnon-pair resonance as a signature of spin-nematic order, *Phys. Rev. B* **102**, 060401(R) (2020).
- [73] A. A. Abrikosov, *Fundamentals of the Theory of Metals*, Dover ed. (Dover, Mineola, NY, 2017).
- [74] A. H. Castro Neto, F. Guinea, N. M. R. Peres, K. S. Novoselov, and A. K. Geim, The electronic properties of graphene, *Rev. Mod. Phys.* **81**, 109 (2009).
- [75] *Physics of Graphene*, NanoScience and Technology, edited by H. Aoki and M. S. Dresselhaus (Springer International, Cham, 2014).
- [76] S. Reich, J. Maultzsch, C. Thomsen, and P. Ordejón, Tight-binding description of graphene, *Phys. Rev. B* **66**, 035412 (2002).
- [77] J. D. Jackson, *Classical Electrodynamics* (Wiley, Weinheim, Germany, 1998).
- [78] E. H. Hwang and S. Das Sarma, Single-particle relaxation time versus transport scattering time in a two-dimensional graphene layer, *Phys. Rev. B* **77**, 195412 (2008).
- [79] R. R. Nair, P. Blake, A. N. Grigorenko, K. S. Novoselov, T. J. Booth, T. Stauber, N. M. R. Peres, and A. K. Geim, Fine structure constant defines visual transparency of graphene, *Science* **320**, 1308 (2008).

- [80] J. Moser, A. Barreiro, and A. Bachtold, Current-induced cleaning of graphene, *Appl. Phys. Lett.* **91**, 163513 (2007).
- [81] O. E. Alon, V. Averbukh, and N. Moiseyev, Selection rules for the high harmonic generation spectra, *Phys. Rev. Lett.* **80**, 3743 (1998).
- [82] T. Morimoto, H. C. Po, and A. Vishwanath, Floquet topological phases protected by time glide symmetry, *Phys. Rev. B* **95**, 195155 (2017).
- [83] K. Chinzei and T. N. Ikeda, Time crystals protected by floquet dynamical symmetry in Hubbard models, *Phys. Rev. Lett.* **125**, 060601 (2020).
- [84] T. N. Ikeda, High-order nonlinear optical response of a twisted bilayer graphene, *Phys. Rev. Res.* **2**, 032015(R) (2020).
- [85] P. Bhalla, K. Das, A. Agarwal, and D. Culcer, Quantum kinetic theory of nonlinear optical currents: Finite Fermi surface and Fermi sea contributions, *Phys. Rev. B* **107**, 165131 (2023).
- [86] S. Ghimire, G. Ndashimiye, A. D. DiChiara, E. Sistrunk, M. I. Stockman, P. Agostini, L. F. DiMauro, and D. A. Reis, Strong-field and attosecond physics in solids, *J. Phys. B* **47**, 204030 (2014).
- [87] H. Haug and A.-P. Jauho, *Quantum Kinetics in Transport and Optics of Semiconductors*, Solid-State Sciences Vol. 123 (Springer, Berlin, 2008).
- [88] M. Tanaka and M. Sato, Theory of the inverse Faraday effect in dissipative Rashba electron systems: Floquet engineering perspective, *Phys. Rev. B* **110**, 045204 (2024).
- [89] D. J. Passos, G. B. Ventura, J. M. Viana Parente Lopes, J. M. B. L. dos Santos, and N. M. R. Peres, Nonlinear optical responses of crystalline systems: Results from a velocity gauge analysis, *Phys. Rev. B* **97**, 235446 (2018).
- [90] Y. Michishita and R. Peters, Effects of renormalization and non-Hermiticity on nonlinear responses in strongly correlated electron systems, *Phys. Rev. B* **103**, 195133 (2021).
- [91] I. Terada, S. Kitamura, H. Watanabe, and H. Ikeda, Unexpected linear conductivity in Landau-Zener model: Limitations and improvements of the relaxation time approximation in the quantum master equation, *Phys. Rev. B* **109**, L180302 (2024).
- [92] G. Stefanucci and R. Van Leeuwen, *Nonequilibrium Many-Body Theory of Quantum Systems: A Modern Introduction*, 1st ed. (Cambridge University Press, Cambridge, 2013).
- [93] P. Bhalla, A. H. MacDonald, and D. Culcer, Resonant photovoltaic effect in doped magnetic semiconductors, *Phys. Rev. Lett.* **124**, 087402 (2020).
- [94] P. Bhalla, K. Das, D. Culcer, and A. Agarwal, Resonant second-harmonic generation as a probe of quantum geometry, *Phys. Rev. Lett.* **129**, 227401 (2022).